

Enhancing SO₃ Hydrolysis and Nucleation: The Role of Formic Sulfuric Anhydride

Rui Wang^a, Rongrong Li^a, Shasha Chen^a, Ruxue Mu^a, Changming Zhang^b,
Xiaohui Ma^{c,*}, Majid Khan^d, Tianlei Zhang^{a,*}

^a Shaanxi Key Laboratory of Catalysis, School of Chemical & Environment Science, Shaanxi University of Technology, Hanzhong, Shaanxi 723001, P. R. China

^b Shaanxi Key Laboratory of Catalysis, School of Mechanical Engineering, Shaanxi University of Technology, Hanzhong, Shaanxi 723001, P. R. China

^c School of Environmental Engineering, Henan University of Technology, Zhengzhou, Henan 450001, China

^d College of Chemistry, Fuzhou University, 350116, Fuzhou, China

Abstract

Although the nucleation route driven by sulfuric acid (H₂SO₄) and ammonia (NH₃) primarily dominates new particle formation (NPF) in the atmosphere, exploring the role of other trace species on H₂SO₄-NH₃ system is crucial for a more comprehensive insight into NPF processes. Formic sulfuric anhydride (FSA) has been observed in atmospheric environment and is found in abundance in atmospheric fine particles. Nevertheless, its effect on SO₃ hydrolysis and NPF remain poorly understood. Here, we studied the enhancing effect of FSA on gaseous and interfacial SO₃ hydrolysis, as well as its impact on H₂SO₄-NH₃-driven NPF occurring through quantum chemical calculations, atmospheric clusters dynamics code (ACDC) kinetics combined with Born-Oppenheimer molecular dynamics (BOMD). Gaseous-phase findings indicate that FSA-catalyzed SO₃ hydrolysis is nearly barrierless. At an [FSA] = 10⁷ molecules·cm⁻³, this reaction competes effectively with SO₃ hydrolysis in the presence of HNO₃ (10⁹ molecules·cm⁻³), HCOOH (10⁸ molecules·cm⁻³) and H₂SO₄ (10⁶ molecules·cm⁻³) in the range of 280.0-320.0 K. At the gas-liquid nanodroplet interface, BOMD simulations reveal that FSA-mediated SO₃ hydrolysis follows a stepwise mechanism, completing within a few picoseconds. Notably, FSA enhances the formation rate of H₂SO₄-NH₃ clusters by over ~~10⁷~~10⁵ times in regions with relatively high [FSA] at elevated temperatures. Additionally, interfacial FSA⁻ ion has the ability to appeal precursor species for particle formation from the gaseous phase to the water nanodroplet interface, thereby facilitating particle growth. These results present new comprehensions into both the pathways of H₂SO₄ formation and aerosol particle growth in polluted boundary layer.

Keywords: gas phase, atmospheric behavior, new particle formation, air pollution

* Corresponding authors. Tel: +86-0916-2641083, Fax: +86-0916-2641083.

e-mail: ztianlei88@163.com (T. L Zhang) and mxhsdu@163.com (X. H Ma)

1. Introduction

Sulfuric acid (SAH_2SO_4) is an important atmospheric pollutant closely associated with new particle formation (NPF) events and is recognized as a vital precursor in the process of converting gases into particles. It facilitates the formation of sulfate aerosols and acid rain in diverse environments, influencing cloud formation, precipitation and the Earth's radiation balance, ultimately contributing to climate change (Yao et al., 2018; Venkataraman et al., 2001; Kumar et al., 2024). Experimental (Couling et al., 2003; Reiner and Arnold, 1993; Bondybey and English, 1985) and theoretical studies (Feng and Wang, 2023; Kumar et al., 2024; Zhang et al., 2025) have shown that atmospheric gaseous $\text{H}_2\text{SO}_4\text{-SA}$ primarily forms via SO_3 hydrolysis (Sarkar et al., 2019; Tao et al., 2018; Carmona-García et al., 2021). However, the likelihood of direct SO_3 hydrolysis in the atmosphere is low due to the high activation energy associated with the process (Chen and Plummer, 1985). Introducing a second water molecule has been shown to significantly lower the activation energy, making SO_3 hydrolysis more efficient (Morokuma and Muguruma, 1994). Further research indicates that, besides water molecules, other species such as formic acid (Kangas et al., 2020), oxalic acid (Yang et al., 2021), nitric acid (Long et al., 2022), $\text{H}_2\text{SO}_4\text{-SA}$ (Wang et al., 2024) and ammonia (Sarkar et al., 2019) exhibit even greater catalytic efficiency in promoting SO_3 hydrolysis for $\text{H}_2\text{SO}_4\text{-SA}$ formation. These findings provide valuable theoretical insights for understanding $\text{H}_2\text{SO}_4\text{-SA}$ sources, particularly in regions where pollutant concentrations are notably elevated. Nevertheless, further investigation is necessary to fully understand the SO_3 hydrolysis mechanism in areas with high levels of specific pollutants, to better assess its behavior and effects under different atmospheric conditions.

Carboxylic sulfuric anhydrides (CSAs) are a recently identified class of atmospheric organosulfides, formed by the cycloaddition of SO_3 with organic carboxylic acids present (Fleig et al., 2012). These CSAs exhibit strong acidity and can act as proton transfer bridges, potentially influencing SO_3 hydrolysis and promoting the formation of $\text{H}_2\text{SO}_4\text{-SA}$ in regions with high CSA concentrations. Research indicates that the gaseous CSA concentration can reach $10^7 \text{ molecules}\cdot\text{cm}^{-3}$ (Smith et al., 2020), creating conditions that may impact SO_3 hydrolysis. As the simplest CSA, formic sulfuric anhydride (FSA) has been characterized using microwave spectroscopic (Mackenzie et al., 2015). FSA is more acidic than formic acid and may facilitate proton transfer in the gaseous

hydrolysis of SO_3 . However, its role in this process has not yet been explored. Besides, it has been reported that the interfacial environment both initiates the organization and clustering of hydrophilic groups and acts as an effective medium for various atmospheric reactions (Ma et al., 2020; Zhong et al., 2019; Tan et al., 2022; Wan et al., 2023). Notably, proton transfer routes induced by interfacial water molecules accelerate numerous atmospheric reactions taking place on aerosols and droplets surfaces. These reactions typically proceed at accelerated rates and can differ from similar processes in the gas phase or bulk water (Tang et al., 2024; Fang et al., 2024; Martins-Costa and Ruiz-López, 2024). Thus, it is essential to investigate whether FSA accelerates SO_3 hydrolysis at the gas-liquid nanodroplet interface, as this could offer valuable insights into atmospheric chemistry and the mechanisms driving particle formation.

Additionally, new species generated from gas-phase reactions of SO_3 with trace substances (Li et al., 2018; Liu et al., 2019) can also significantly influence the NPF process. For example, Li et al. (Li et al., 2018) revealed that $\text{NH}_2\text{SO}_3\text{H}$, formed from the reaction of SO_3 with ammonia (A) NH_3 , not only contributes directly to $\text{H}_2\text{SO}_4\text{SA}-(\text{CH}_3)_2\text{NH}$ cluster formation but also enhances the maximum rate of NPF from $\text{H}_2\text{SO}_4\text{SA}$ and $(\text{CH}_3)_2\text{NH}$ by approximately twofold in heavily polluted areas with high concentrations of basic substances. Similarly, Liu et al. (Liu et al., 2019) predicted that methyl hydrogen sulfate (MHS), formed from the reaction of SO_3 with methanol, significantly impacts $\text{H}_2\text{SO}_4\text{SA}-(\text{CH}_3)_2\text{NH}$ nucleation, particularly in dry regions with high alcohol concentrations. FSA, produced from the reaction of SO_3 with HCOOH , contains the $-\text{OSO}_3\text{H}$ functional group and exhibits a binding capability comparable to that of $\text{H}_2\text{SO}_4\text{SA}$ with nucleation precursors like NH_3A . The potential role of FSA in enhancing $\text{H}_2\text{SO}_4\text{SA}-\text{NH}_3\text{A}$ nucleation in the atmosphere requires further investigation to fully understand its contribution to NPF processes.

This work examined the catalytic effect of FSA on SO_3 hydrolysis and $\text{H}_2\text{SO}_4\text{SA}-\text{NH}_3\text{A}$ nucleation particle formation. Specifically, the catalytic effects of FSA on gaseous SO_3 hydrolysis were firstly explored. Following this, the differences between the gaseous and interfacial reactions of FSA-catalyzed SO_3 hydrolysis were evaluated using BOMD simulations. Subsequently, a qualitative evaluation of FSA's nucleation capability was conducted through molecular dynamics (MD) simulations. Finally, the atmospheric implications of FSA on particle formation were analyzed. This study not only deepens our understanding of the impact of FSA on SO_3 hydrolysis but also provides new molecular-level mechanisms for the contribution to $\text{H}_2\text{SO}_4\text{SA}-\text{NH}_3\text{A}$ particle

formation.

2. Computational Methods

2.1 Quantum Chemical Details. The M06-2X functional (Mardirossian and Head, 2016; Pereira et al., 2017) is highly effective in describing noncovalent interactions and estimating the thermochemistry and equilibrium structures of atmospheric reactions. To investigate the impact of formic sulfuric anhydride (FSA) on gaseous SO₃ hydrolysis, the M06-2X/6-311++G(2df,2pd) computational method, as implemented in Gaussian 09 software (Frisch, 2009), was employed to analyze the geometric structures and vibrational frequencies of the relevant species. It is noted that the calculated bond distances and bond angles at the M06-2X/6-311++G(2df,2pd) level (Fig. S1) are in good agreement with both experimental data and values obtained using the M06-2X/6-311++G(3df,3pd) method. ~~We also carried out~~ Meanwhile, the calculation of intrinsic reaction coordinate to conduct the connections between the transition states and their corresponding pre-reactive and post-reactive complexes. To enhance the reliability of the relative Gibbs free energies, single-point energies at the CCSD(T)-F12/cc-pVDZ-F12-CABS ~~CCSD(T)-F12/cc-pVDZ-F12~~ level were calculated using the ORCA software (Neese, 2012).

The most stable structure of the (FSA)_x(SA)_y(A)_z ($z \leq x + y \leq 3$) clusters were obtained by the following three steps. Initially, the ABCluster program (Zhang and Dolg, 2015) was utilized to randomly produce $n \times 1000$ initial isomers ($1 \leq n \leq 3$) ~~(where $n = 2$ to 4)~~, which were subsequently evaluated using the PM6 method via MOPAC 2016 (Partanen et al., 2016). Next, up to $n \times 100$ lowest-energy isomers were chosen and further refined using the method of M06-2X/6-31+G(~~df,pp~~). ~~Then~~ Lastly, the top $n \times 10$ isomers were re-optimized at the M06-2X/6-311++G(2df,2pd) method level to ascertain their isomers with the lowest energy. Lastly, based on the optimized geometries of the stable clusters at the M06-2X/6-311++G(2df,2pd) level, the single point energies were calculated at the DLPNO-CCSD(T)-F12/cc-pVDZ-F12-CABS level (Tchinda et al., 2022) using the ORCA. The optimized structures and their Gibbs free energies are detailed in Fig. ~~S1240~~ and Table ~~S76~~, respectively.

2.2 Rate Coefficient Computations. Rate coefficients for FSA-assisted SO₃ hydrolysis were calculated via two steps as follows. First, the VRC-VTST methodology (Zhang et al., 2023; Zhang

et al., 2024) was applied using the Polyrate program (Meana-Pañeda et al., 2024) to calculate the rate coefficients under high-pressure conditions. Next, the Master Equation Solver for Multi-Energy Well Reactions (Glowacki et al., 2012) was engaged in computing the rate coefficients for FSA-assisted SO_3 hydrolysis across a temperature range of 280.0 to 320.0 K. To estimate the rate coefficients for the barrier less formation of pre-reactive complexes from the separated reactants, we applied the Inverse Laplace Transform (ILT) method (Kumar et al., 2021). In parallel, RRKM theory (Bao et al., 2016) was utilized to estimate the rate coefficients for the transition from the pre-reactive complex to the post-reactive complex through a transition state. Additionally, the MESMER calculations in this study applied an Eckart tunneling correction to the reaction rates. Details of the ILT methods and RRKM theory are provided in Part 1 and Part 2 in the Supplement, respectively.

2.3 BOMD Simulations. BOMD simulations were conducted with the CP2K program (Hutter et al., 2014). The BLYP functional was applied to address exchange and correlation interactions (Becke, 1988; Lee et al., 1988). Grimme's dispersion-corrected method (Grimme et al., 2010) was employed to account for the dispersion interactions and effectively handle weak dispersion effects. The GTH norm-conserving pseudopotentials (Goedecker et al., 1996), along with the Gaussian DZVP basis set (Phillips et al., 2005) and the auxiliary plane wave basis set, were utilized to describe the core and valence electrons, respectively. The Goedecker-Teter-Hutter conservation pseudopotentials (Goedecker et al., 1996) were done by using Gaussian DZVP basis set (Phillips et al., 2005) and an auxiliary plane wave basis, ensuring accurate treatment of both valence and core electrons. The plane wave basis set was established with a 280 Ry energy cutoff, while the Gaussian basis set cutoff was set at 40 Ry. A supercell side length of 15 Å was used in gas phase simulations to eliminate periodic boundary conditions with step of 0.5 fs. For interfacial reactions, a water droplet containing 191 water molecules was initially pre-optimized through BOMD simulation for approximately 5.0 ps at 300 K. Subsequently, SO_3 and FSA were positioned at the gas-liquid nanodroplet interface to perform the simulations over 10 ps. A supercell side length of 35 Å was set for gas-liquid nanodroplet interface simulations to prevent periodic interactions between neighbouring water droplets, using a step of 1.0 fs. In all simulations under the NVT ensemble, a stable temperature of 300 K was maintained using the Nose-Hoover thermostat.

2.4 Classical Molecular Dynamics Simulation ~~Molecular Dynamics Simulation of~~

Nucleation.

MD simulations were conducted using the GROMACS 2024.3 software package (Abraham et al., 2024) with the general AMBER force field (GAFF). GAFF is a comprehensive force field that encompasses nearly all of organic chemical space, including elements such as C, N, O, S, P, H, F, Cl, Br, and I. This force field has been widely utilized in studies of the air-water interface, with the results confirming its suitability for predicting the properties of species at this interface (Li et al., 2024b; Cheng et al., 2025; Zhao et al., 2019). To get the force field parameters, geometry optimization at the M06-2X/6-311++G(2df,2pd) level were performed, following Electrostatic potential (ESP) calculations at the same level. Geometry optimization and electrostatic potential (ESP) calculations were carried out with the Gaussian 09 software. The restrained electrostatic potential (RESP) charges were calculated using Multiwfn 3.8 (dev) (Lu and Chen, 2012). Subsequently, the AMBER parameter and coordinate files were generated using Packmol (Martínez et al., 2009) and Sobtop (Lu, 2023), respectively.

2.4.1 Surface preference of SO₃, FSA and SO₃-FSA

A cubic box with a side length of 4 nm, containing 2165 water molecules, was initially constructed. The box was then extended along the z-axis to a length of 9 nm. The water slab was positioned at the center of the box with the COM coordinates of (2.0 nm, 2.0 nm, 4.5 nm), while the SO₃, FSA and SO₃-FSA complexes were placed at (2.0 nm, 2.0 nm, 7.5 nm) (Fig. S6(c)). Subsequently, a 150 ns NVT simulation was conducted.

2.4.2 Molecular Dynamics Simulation of Nucleation

~~Complete nucleation pathway was simulated using the GROMACS 2024.3 software (Abraham et al., 2024), employing the general AMBER force field, a widely utilized approach for modelling molecular dynamics (Li et al., 2024b; Cheng et al., 2025; Zhao et al., 2019). The electrostatic potential was computed at M06-2X/6-311++G(2df,2pd) level and the restrained electrostatic potential charges were determined using Multiwfn 3.8 (Lu and Chen, 2012). The AMBER parameter and coordinate files were constructed using Sobtop (Lu, 2023) and Packmol (Martínez et al., 2009), respectively.~~ The simulation was performed within a cubic simulation box, each side measuring 200 Å in length. Following energy minimization, the system was further simulated under the NVT and NPT ensembles at 298 K for durations of 100 ps and 40 ns, respectively. The Berendsen pressure coupling method (Berendsen et al., 1984) and the velocity

rescaling thermostat (Bussi et al., 2007) were used to regulate pressure and temperature, respectively. The system applied periodic boundary conditions to mimic an infinite environment, with a 1 fs time step. The electrostatic and van der Waals interactions were set with a 1.4 nm cutoff distance, and the Particle-Mesh Ewald method (York et al., 1993) was implemented for long-range electrostatics.

~~All the bond lengths were restricted by the LINCS algorithm (Hess et al., 1997) to preserve structural integrity during the simulation. Bond lengths were restricted by the LINCS algorithm (Hess et al., 1997) to preserve structural integrity during the simulation.~~

2.5 Atmospheric Cluster Dynamics Code (ACDC) Model. The ACDC (McGrath et al., 2012) was employed to investigate cluster formation rates and growth mechanisms for $(\text{FSA})_x(\text{SA})_y(\text{A})_z$ clusters. The ACDC simulations were supplied with thermodynamic data, which was derived from quantum chemical calculations performed by M06-2X/6-311++G(2df,2pdpd). Accounting for all potential collision and evaporation processes, the following formulation represents the birth-death equations:

$$\frac{dc_i}{dt} = \frac{1}{2} \sum_{j < i} \beta_{j,(i-j)} C_j C_{(i-j)} + \sum_j \gamma_{(i+j) \rightarrow i} C_{i+j} - \sum_j \beta_{i,j} C_i C_j - \frac{1}{2} \sum_{j < i} \gamma_{i \rightarrow j} C_i + Q_i - S_i \quad (1)$$

In the above equation, c_i represents the concentration of i cluster, while β_{ij} stands for the collision ~~coefficient rate~~ between i and j clusters. The term $\gamma_{(i+j) \rightarrow i}$ refers to the ~~coefficient rate~~ at which the larger $i+j$ cluster breaks down (or evaporates) into i and j clusters. Additionally, Q_i accounts for any possible external source of i cluster. To consider the external losses of i cluster, a coagulation sink coefficient of $2 \times 10^{-2} \text{ s}^{-1}$ was used, aligning with values typically found in polluted environments (Liu et al., 2021b). In ACDC, boundary clusters must be sufficiently stable, which allows them to continue growing. ~~Therefore, the clusters of $(\text{SA})_4 \cdot (\text{A})_3$, $(\text{SA})_4 \cdot (\text{A})_4$, $(\text{FSA})_4 \cdot (\text{A})_3$, $(\text{FSA})_4 \cdot (\text{A})_4$, $(\text{FSA})_3 \cdot \text{SA} \cdot (\text{A})_3$, $(\text{FSA})_2 \cdot (\text{SA})_2 \cdot (\text{A})_3$ and $\text{FSA} \cdot (\text{SA})_3 \cdot (\text{A})_3$ were selected as the boundary clusters in the SA-A-FSA system. Therefore, the clusters of $(\text{FSA})_2 \cdot (\text{SA})_2 \cdot (\text{A})_3$, $(\text{FSA})_1 \cdot (\text{SA})_3 \cdot (\text{A})_3$, $(\text{SA})_4 \cdot (\text{A})_3$ and $(\text{SA})_4 \cdot (\text{A})_4$ were selected as the boundary clusters in the SA-A-FSA system.~~

3. Results and discussion

3.1 The Hydrolysis of SO_3 Assisted by FSA

The SO_3 hydrolysis with HCOOSO_3H (FSA) can initially occur via the interaction between

SO₃ (or FSA) and H₂O to form SO₃···H₂O (or FSA···H₂O) dimer. Subsequently, the SO₃···H₂O dimer collides with FSA, and the FSA···H₂O dimer interacts with SO₃. The predicted relative Gibbs free energies of SO₃···H₂O ~~was~~is 0.8 kcal·mol⁻¹ at the CCSD(T)-F12/cc-pVDZ-F12//M06-2X/6-311++G(2~~df,2p~~~~df,2p~~) level, which is nearly previously reported values (-0.2 to 1.0 kcal·mol⁻¹) (Long et al., 2013; Long et al., 2012; Lv et al., 2019; Bandyopadhyay et al., 2017). As compared with FSA···H₂O, the binding free energy of SO₃···H₂O is less stable by 2.6 kcal·mol⁻¹, which leads to the equilibrium coefficient of FSA···H₂O (2.63×10^{-18} - 2.49×10^{-19} molecules·cm⁻³) (Table S2) being at least 10 times larger than that of SO₃···H₂O (2.45×10^{-20} - 5.10×10^{-21} molecules·cm⁻³ within 280.0-320.0 K). Under the available concentrations ([FSA] = 1.0×10^7 , [SO₃] = 1.0×10^3 molecules·cm⁻³) (Liu et al., 2019), the concentration of FSA···H₂O is 1.36×10^6 - 6.80×10^6 molecules·cm⁻³ within 280.0-320.0 K, which is 10⁶ times larger than that of SO₃···H₂O (Table S3). Therefore, it is predicted that SO₃ hydrolysis with FSA predominantly take places via the collision between FSA···H₂O and SO₃.

Starting from the FSA···H₂O + SO₃ reactants, an eight-membered ring pre-reactive complex SO₃···H₂O···FSA (named as IM_{SA_FSA}) ~~was~~is found and its Gibbs free energy relative to the isolated SO₃, H₂O and FSA reactants ~~was~~is -2.0 kcal·mol⁻¹. In comparison to the previously reported neutral (SO₃···2H₂O) and acidic complexes SO₃···H₂O···X (X = HNO₃, HCOOH, (COOH)₂ and H₂SO₄) (Yang et al., 2021; Long et al., 2012; Torrent-Sucarrat et al., 2012; Long et al., 2013), the stability of the SO₃···H₂O···FSA complex is notably enhanced by 0.2-2.7 kcal·mol⁻¹. This is because the positive electrostatic potential (ESP) of the hydrogen atom in the FSA molecule (Fig. ~~S4~~S5) is stronger than those in H₂O and X molecules, resulting in stronger intermolecular interactions of SO₃···H₂O···FSA. Following the IM_{SA_FSA} complex, the reaction proceeds via TS_{SA_FSA}, leading to the H₂SO₄···FSA formation. For the FSA-catalyzed SO₃ hydrolysis, its Gibbs free energy barrier is 2.5 kcal·mol⁻¹, representing a reduction of 22.1 kcal·mol⁻¹ relative to the SO₃ hydrolysis without FSA (Table S1). Moreover, it is also 1.0-4.0 kcal·mol⁻¹ lower in free energy barrier than those of the SO₃ hydrolysis with H₂O, HNO₃ and H₂SO₄ (Table S1). Therefore, FSA is clearly more effective than H₂O, HNO₃ and H₂SO₄ in decreasing the energy barrier for SO₃ hydrolysis. H₂SO₄···FSA is an eight-membered ring complex, similar to H₂SO₄···X complexes in the SO₃ hydrolysis with X. The predicted free energy of H₂SO₄···FSA (-12.9 kcal·mol⁻¹) is lower by 10.9 kcal·mol⁻¹ compared to that of the IM_{SA_FSA} complex. This indicates the thermodynamic favorability of FSA-assisted SO₃

hydrolysis.

The computed rate coefficients for the hydrolysis of SO_3 with and without FSA, H_2O and X within 280.0-320.0 K are shown in Table 1. As observed at 298.0 K, the rate coefficient for the SO_3 hydrolysis with FSA (k_{FSA}) is $7.71 \times 10^{-11} \text{ cm}^3 \cdot \text{molecule}^{-1} \cdot \text{s}^{-1}$, surpassing that of the uncatalyzed SO_3 hydrolysis by a factor of 10^{12} . Additionally, the value of k_{FSA} at 298.0 K is larger by factors of 60.23 and 84.63 than those for the SO_3 hydrolysis with H_2O (k_{WM}) and HNO_3 (k_{NA}), respectively. Similarly, within 280.0-320.0 K in Table 1, FSA can compete with HCOOH , $(\text{COOH})_2$ and H_2SO_4 with the value of k_{FSA} being larger by factors of 1.02-1.64 than those of k_{FA} , k_{OA} and k_{SA} . These findings indicate that the catalytic efficiency of FSA in SO_3 hydrolysis surpasses that of H_2O and HNO_3 , and is comparable to HCOOH , $(\text{COOH})_2$ and H_2SO_4 .

To consider a contribution of FSA on SO_3 hydrolysis, the rate ratios between FSA- and X -catalyzed SO_3 hydrolysis reactions were calculated, as shown in Table S5. As observed, the SO_3 hydrolysis with H_2O is more favorable than with FSA because the $[\text{H}_2\text{O}]$ (10^{16} - $10^{18} \text{ molecules} \cdot \text{cm}^{-3}$) is significantly greater than $[\text{FSA}]$ ($10^7 \text{ molecules} \cdot \text{cm}^{-3}$). When the acid catalysts HNO_3 ($10^9 \text{ molecules} \cdot \text{cm}^{-3}$), HCOOH ($10^8 \text{ molecules} \cdot \text{cm}^{-3}$) and SA ($10^6 \text{ molecules} \cdot \text{cm}^{-3}$) are considered, FSA dominates over them within 280.0-320.0 K as the rate ratio v_{WM}/v_X is greater than 1. This reveals that the FSA-assisted reaction is indispensable in SO_3 hydrolysis within regions affected by FSA pollution and can significantly promote the hydrolysis of SO_3 within 280.0-320.0 K.

3.2 FSA-Catalyzed SO_3 Hydrolysis at the Gas-liquid Nanodroplet Interface

Aqueous interfaces are widespread across Earth's atmosphere. (Li et al., 2024a; Zhong et al., 2017; Sun et al., 2024; Gao et al., 2024; Dong et al., 2024). The gas-liquid nanodroplet interface serves as a significant site for adsorption and reactions, potentially enhancing atmospheric reaction rates and leading to the emergence of novel mechanisms. However, at the gas-liquid nanodroplet interface, comprehensive understanding of the mechanism for FSA-assisted SO_3 hydrolysis was lacking. Notably, during the 150 ns simulation, SO_3 , the FSA molecule and the SO_3 -FSA complex were observed to reside at the interface for 35.8%, 46.3% and 40.5% (Fig. S5S7), respectively, revealing that the presence of SO_3 , FSA molecule and SO_3 -FSA complex cannot be ignored at the gas-liquid nanodroplet interface. To further investigate this prediction, we performed BOMD simulations to assess the FSA-assisted hydrolysis of SO_3 at the gas-liquid nanodroplet interface. Similar to the reactions of SO_3 with other acidic species at this interface, the interaction between

SO₃ and FSA at the aqueous interface might take place via three pathways: (i) direct interaction of SO₃ with adsorbed FSA; (ii) interaction of adsorbed SO₃ with FSA; or (iii) reaction starting from the SO₃-FSA complex. Given the high reactivity and the brief residency time of SO₃ and FSA at the interface, as evidenced by their short lifetimes (Fig. S6S8) of only a few picoseconds and rapid formation of SA⁻ and FSA⁻ ion, the simulations have primarily considered the model of (iii). Notably, the contribution of pathway (iii) on the aqueous nanodroplet surface is slight due to the low concentration of SO₃-FSA complex (9.49×10^{-23} - 1.80×10^{-22} molecules·cm⁻³ within 280.0-320.0 K (Table S2)). This focus enabled a deeper understanding of the interfacial dynamics and the mechanisms underpinning these rapid transformations.

Unlike the gaseous hydrolysis mechanism of SO₃ with FSA, which occurs through the one-step mechanism, interfacial SO₃ hydrolysis mediated by FSA occurs via a stepwise mechanism (Fig. 2, Fig. S7-S9 and Movie S1), consisting of three steps: i) SO₃ hydrolysis along with proton transfer outside the ring; ii) the deprotonation of FSA; and iii) the deprotonation of H₂SO₄. Specifically, at 0 ps, a loop-structure complex, SO₃···(H₂O)₂···FSA, was initially found with the formations of three hydrogen bonds ($d_{(O6\cdots H4)} = 1.75$; $d_{(O3\cdots H2)} = 1.92$ and $d_{(O5\cdots H3)} = 2.39$ Å) and a van der Waals interaction ($d_{(O1\cdots S)} = 2.31$ Å). Then, the loop structure mechanism proceeded along with the simultaneous event of the proton transfer outside the ring. At 1.01 ps, an arrangement resembling a transition state was found for the interfacial SO₃ hydrolysis, characterized by shortening of the S-O1 and O2-H1 bonds and elongation of the O1-H1 bond. By 1.14 ps, the S-O1 and O2-H1 bond lengths had reduced to 1.45 Å and 0.97 Å, respectively, while the O1-H1 bond had elongated to 1.42 Å, indicating the formation of HSO₄⁻ and H₃O⁺ ions. Due to the strong acidity of FSA, the H3 atom of FSA was moved to the O5 atom of the HSO₄⁻ ion at 1.87 ps, leading to H₂SO₄ molecule and FSA⁻ ion. Finally, the deprotonation of H₂SO₄ was completed at 2.18 ps, with the H2 atom of H₂SO₄ moved to one interfacial water molecule inside the ring. In contrast to the SO₃ hydrolysis with FSA in the gas phase, which does not proceed within 100 ps, the reaction at the gas-liquid nanodroplet interface rapidly proceeds within just a few picoseconds. ~~This indicates that interfacial water molecules at the gas-liquid nanodroplet interface can accelerate the SO₃ hydrolysis. However,~~ considering the harsh reaction conditions between SO₃ and FSA at the interface (i.e., the two molecules must be sufficiently close to formed the SO₃-FSA complex) and the high concentration of water molecules at the aqueous interfaces, the direct hydrolysis of SO₃ at the aqueous interfaces

is more advantageous than the $\text{SO}_3\text{-FSA}$ complex reacting on the aqueous surface.

Interestingly, the formation of FSA^- and HSO_4^- is highly stable, and their dissociation did not occur within 10 ps. Species such as H_2SO_4 (SA), NH_3 (A), HNO_3 , and $(\text{COOH})_2$ are identified as candidates for particle formation, with the SA-A cluster serving as a significant precursor to atmospheric aerosols. Calculated binding free energies of the corresponding bimolecular clusters were shown in Table 2 where the computed binding free energies agree well with previous values (Zhong et al., 2019). As shown, the interactions of FSA^- -SA ($-21.2 \text{ kcal}\cdot\text{mol}^{-1}$) and FSA^- - HNO_3 ($-12.1 \text{ kcal}\cdot\text{mol}^{-1}$) are stronger than that of SA-A ($-8.9 \text{ kcal}\cdot\text{mol}^{-1}$), illustrating that interfacial FSA^- and H_3O^+ ions can attract precursor molecules from the gaseous phase to the aqueous nanodroplet surface, and thus facilitating particle growth. Additionally, the enhancing potential of the FSA^- ion on the SA-A cluster was assessed by examining the binding free energies of the SA-A- FSA^- and SA-A-Y ($Y = \text{HOOCCH}_2\text{COOH}$, $\text{HOCCOOSO}_3\text{H}$, $\text{CH}_3\text{OSO}_3\text{H}$, $\text{HOOCCH}_2\text{CH}(\text{NH}_2)\text{COOH}$ and HOCH_2COOH) clusters. The binding free energies of SA-A- FSA^- and SA-A-Y clusters listed in Table 2 were consistent with previously reported values (Rong et al., 2020; Zhang et al., 2018; Zhang et al., 2017; Gao et al., 2023; Liu et al., 2021a). Notably, compared to SA-A-Y, the binding free energy of SA-A- FSA^- ($-25.6 \text{ kcal}\cdot\text{mol}^{-1}$) was larger than $5.2\text{-}12.8 \text{ kcal}\cdot\text{mol}^{-1}$, indicating that the FSA^- at the interface exhibits a greater nucleation capability than gaseous molecule Y. Consequently, FSA^- is expected to demonstrate enhanced nucleation potential at the gas-liquid interface. A further quantitative assessment of the aerosol nucleation potential of Y ions at the droplet interface could not be conducted, as data on the concentration of Y ions at the interface are not yet available.

3.3 FSA's Role in Nucleation and Cluster Formation

Electrostatic potential (ESP) analysis was conducted to predict the potential hydrogen bond binding sites among FSA, SA and A. The -OH moiety in the FSA molecule contains a highly electrophilic hydrogen atom, making it a favorable donor site for hydrogen bonds (ESP value: $+60.6 \text{ kcal}\cdot\text{mol}^{-1}$) (Fig. 3). Meanwhile, the terminal oxygen atoms of the - SO_3H and - COOH moieties in FSA can act as an effective hydrogen bond receptor site due to their stronger electronegativity (ESP values: -23.8 , -22.4 and $-13.0 \text{ kcal}\cdot\text{mol}^{-1}$). Thus, FSA can form stable clusters by forming hydrogen bonds with SA and A.

Using MD simulations, the aggregation behavior of FSA with SA and A molecules was investigated at various atmospheric temperatures (Fig. 4 and Figs. S8S10-S9S11). In these

simulation systems, 5 FSA, 5 SA, 10 A, 20 H₂O, 41 O₂ and 154 N₂ molecules were included. Similar with the previously studies (Ding et al., 2024; Wei et al., 2022; Li et al., 2023), the concentration of precursors has not been considered, and only a qualitative assessment of FSA's involvement in SA-A nucleation was conducted. Notably, the complete stable (FSA)₅•(SA)₅•(A)₁₀ cluster was observed at all the three simulations temperatures. ~~With rising temperatures, the aggregation time for the formation of (FSA)₅•(SA)₅•(A)₁₀ cluster (Fig. 4(a)) increases. This observed phenomenon of aggregation implies that lower temperatures are more conducive to form the (FSA)₅•(SA)₅•(A)₁₀ cluster.~~ Fig. 4(b) displayed the snapshots of the nucleation simulation at 258.15 K. The initial simulation at 0 ns shows that there is not effective nucleation, as all molecules in the system are scattered (Fig. 4(b)). ~~Subsequently, FSA can bind with SA and A to form FSA•A, FSA•SA•A and FSA•SA•(A)₃ clusters at 1.5 ns, and then the FSA•SA•A, (FSA)₂•SA•(A)₃ and (FSA)₂•(SA)₂•(A)₃ clusters are formed at 3.0 ns. Next, with further aggregation of FSA molecules, (FSA)₂•SA•(A)₄ and (FSA)₃•(SA)₃•(A)₄ clusters are observed within 4.0 ns. Finally, the FSA molecules fully aggregate to form (FSA)₅•(SA)₅•(A)₁₀ clusters at 7.5 ns, and this complete cluster stays stable throughout the entire simulation period.~~ Subsequently, at 0.4 ns, various clusters such as SA•A and FSA•A clusters were formed. As molecular aggregation continued, the collision between FSA, SA, and A molecules results in the formation of SA•(A)₂, FSA•A, FSA•SA•A and FSA•SA•(A)₃ clusters at 1.5 ns, and then the SA•(A)₂, FSA•SA•A, (FSA)₂•SA•(A)₃ and (FSA)₂•(SA)₂•(A)₃ clusters are formed at 3.0 ns. Next, with further aggregation of the molecules, SA•(A)₂, (FSA)₂•SA•(A)₄ and (FSA)₃•(SA)₃•(A)₄ clusters are observed within 4.0 ns. Finally, the molecules fully aggregate to form (FSA)₅•(SA)₅•(A)₁₀ clusters at 7.5 ns, and this complete cluster stays stable throughout the entire simulation period. It is noteworthy that the numbers of FSA molecules can gradually interact with SA and A molecules to form relatively large clusters, where hydrogen bonds among SA, A and FSA play a crucial role. ~~Therefore, it is initially predicted that FSA could act as a “participator” in NPF and could be directly involved in SA-A nucleation. Further predictions regarding for the enhancement effect of FSA on SA-A molecular clustering have been studied by considering the cluster stability, the formation rate and the growth pathways.~~ It is also noteworthy that during the nucleation process, the proton transfer between acid and base molecules plays an important role in acid-base nucleation which cannot be reflected in the classical MD simulation. However, it is initially predicted by classical MD simulation that FSA could act as a “participator” in NPF and

could be directly involved in SA-A nucleation. Further predictions regarding the enhancement effect of FSA on SA-A molecular clustering should be conducted below by considering the cluster stability, the formation rate and the growth pathways.

3.4 The Impact of Atmospheric Conditions on the Thermodynamic Clusters Stability

The Gibbs free energies of formation (ΔG , kcal·mol⁻¹) and evaporation rate coefficients (γ , s⁻¹) of the (FSA)_x(SA)_y(A)_z clusters were analyzed to estimate the thermodynamic stability of the clusters involved in the SA-A-FSA system (Tables S6S7-S7S8). The ΔG and γ of the important pure SA·A clusters and FSA-containing stable clusters were primarily discussed at three temperature. At 298.15 K, the ΔG value of the SA·A cluster was ~~2.692.1~~ kcal·mol⁻¹ greater than that of the FSA·A cluster (Fig. 5). Meanwhile, its γ value was about ~~4010²~~ times greater than that of the FSA·A cluster, suggesting that the FSA·A cluster is more stable and likely to participate in subsequent growth as an initial cluster. For the (FSA)₂·(A)₂ cluster, its ΔG (~~-31.41-31.1~~ kcal·mol⁻¹) was smaller by ~~3.504.6~~ kcal·mol⁻¹ than that of the (SA)₂·(A)₂ cluster (~~-26.5-27.91~~ kcal·mol⁻¹) with the γ value of the former one (~~5.34 × 10¹2.48~~ s⁻¹) at least 10⁴ times lower than that of the latter one (~~6.138.35 × 10⁴10⁵~~ s⁻¹), indicating that the (FSA)₂·(A)₂ cluster is more stable than clusters containing SA and A with the same acid-base number. For the (FSA)₃·(A)₃ cluster, its γ (~~3.303.33 × 10⁻¹10⁻³~~ s⁻¹) was nearly 10⁵³ times lower than that of the (SA)₃·(A)₃ (~~2.25-1.11 × 10²~~ s⁻¹) cluster, allowing (FSA)₃·(A)₃ to serve as a critical nucleation cluster and participate in subsequent growth. Similarly, at 278.15 K and 258.15 K, the FSA·A, (FSA)₂·(A)₂ and (FSA)₃·(A)₃ clusters were all more stable than the SA-A binary nucleation clusters with the same acid-base number. Regarding for the (FSA)₂·SA·(A)₃ and FSA·(SA)₂·(A)₃ clusters at 298.15 K, the ΔG values (~~-56.7-57.73~~ and ~~-54.1-54.83~~ kcal·mol⁻¹) were lower than that of (SA)₃·(A)₃ (~~-52.0-53.69~~ kcal·mol⁻¹). Simultaneously, the γ values of the (FSA)₂·SA·(A)₃ (~~8.493.38 × 10⁻⁵10⁻⁴~~ s⁻¹) and FSA·(SA)₂·(A)₃ (~~5.285.75 × 10¹~~ s⁻¹) clusters were respectively lower 10⁶ and ~~10-2~~ times lower than that of (SA)₃·(A)₃ (~~2.251.11 × 10²~~ s⁻¹). Likewise, the (FSA)₂·SA·(A)₃ and FSA·(SA)₂·(A)₃ clusters were more stable than the (SA)₃·(A)₃ cluster at low temperatures (278.15 K and 258.15 K) due to their significantly lower evaporation rates. Therefore, compared to pure SA-A clusters, clusters containing FSA molecules exhibit higher stability and are more likely to engage in nucleation and subsequent cluster growth processes as stable clusters. ~~The clusters of (SA)₃·(A)₃, (FSA)₂·SA·(A)₃ and FSA·(SA)₂·(A)₃ have the potential~~

to further grow into the boundary clusters $[(\text{FSA})_2(\text{SA})_2(\text{A})_3, (\text{FSA})_4(\text{SA})_3(\text{A})_3, (\text{SA})_4(\text{A})_3$ and $(\text{SA})_4(\text{A})_4]$. The clusters of $(\text{SA})_3(\text{A})_3$, $(\text{FSA})_3(\text{A})_3$, $(\text{FSA})_2\text{SA}(\text{A})_3$ and $\text{FSA}(\text{SA})_2(\text{A})_3$ have the potential to further grow into the boundary clusters $[(\text{SA})_4(\text{A})_3, (\text{SA})_4(\text{A})_4, (\text{FSA})_4(\text{A})_3, (\text{FSA})_4(\text{A})_4, (\text{FSA})_3\text{SA}(\text{A})_3, (\text{FSA})_2(\text{SA})_2(\text{A})_3$ and $\text{FSA}(\text{SA})_3(\text{A})_3]$, which has relative lower Gibbs free energy and evaporation rates.

3.5 Influence of Particle Formation Rates Under Varying Temperatures and Nucleation Precursor Concentrations

To investigate the cluster formation rate (J , $\text{cm}^{-3}\cdot\text{s}^{-1}$) and the enhancement factor (R) of cluster formation rate by FSA, a range of ACDC simulations were performed using thermodynamic data for the SA-A-FSA clusters at varying temperatures and monomer concentrations ($[\text{SA}] = 10^4 - 10^8$, $[\text{A}] = 10^7 - 10^{11}$ and $[\text{FSA}] = 10^3 - 10^7$ molecules $\cdot\text{cm}^{-3}$). The value of R is defined as $R = J_{\text{SA-A-FSA}}/J_{\text{SA-A}}$. The values of J and R for the SA-A-FSA system at varying temperatures (Fig. 6) showed that J increased as the temperature decreased, due to the smaller values of both ΔG and γ at lower temperatures. Meanwhile, J increased with increasing $[\text{FSA}]$, attributable to the formation of more SA-A-FSA clusters. Variations in $[\text{FSA}]$ and temperature can also affect R . A significant increase in R with the rising $[\text{FSA}]$ has been observed, suggesting that FSA can strongly enhance the nucleation rate in SA-A NPF. Interestingly, as the temperature increases (Fig. 6(b)), the value of R becomes greater. In summary, the inclusion of FSA can substantially improve J for SA-A nucleation in regions with relatively high $[\text{FSA}]$ during summer or at lower altitudes with high temperatures.

In addition to temperature and $[\text{FSA}]$, J and R can also be affected by $[\text{SA}]$ and $[\text{A}]$. At 278.15 K, J increased with increase of $[\text{SA}]$ or $[\text{A}]$ (Fig. 7(a)). Nevertheless, R decreased with increasing $[\text{SA}]$ (Fig. 7(b)). This trend may be due to both FSA and SA are acidic molecules, creating a competitive relationship when they interact with A. Additionally, the changes in J with $[\text{SA}]$ or $[\text{A}]$ and R with $[\text{SA}]$ were similar at other temperatures of 258.15 K and 298.15 K. Similar negative dependencies between R and $[\text{A}]$ were observed at both 278.15 K and 298.15 K. This occurs because, as the $[\text{A}]$ increases, the interaction between FSA and SA in the SA-A-FSA system may be disrupted, leading to a decrease in the saturation of FSA interaction sites and a reduction in R . Notably, at the lower temperature of 258.15 K, when $[\text{FSA}]$ was high, the value of R initially decreased and then increased with increasing $[\text{A}]$ (as depicted in Fig. S12 (b)). This may be attributed to the following reasons. First, as $[\text{A}]$ increases, the interaction between FSA and SA in the ternary cluster may be

disrupted, leading to a decrease in the saturation of FSA interaction sites and a reduction in R . Then, as the concentration of A further increases, excess A molecules bind to FSA molecules, leading to an increase in R . In summary, FSA primarily enhances SA-A nucleation in regions with higher temperatures and lower [A] and [SA]. Specifically, when [FSA] ranges from 10^3 to 10^7 molecules·cm⁻³, J can increase by up to four orders of magnitude at 258.15 K. At 298.15 K, J shows a significant increase, rising by five orders of magnitude. These findings suggest that the formation rate exhibits a substantial variation at high temperatures. Meanwhile, J increased with increasing [FSA], attributable to the formation of more SA-A-FSA clusters. For example, when [FSA] exceeds 10^3 molecules·cm⁻³ at the high temperature of 298.15 K, J exhibits a significant increase, rising by five orders of magnitude. This suggests that the involvement of FSA can strongly enhance the nucleation rate in SA-A-based NPF. In addition to temperature and [FSA], the varying concentrations of SA and A might have a significant impact on the nucleation rate. Fig. 7 reveals a clear positive correlation between J and both [SA] and [A]. This can also be attributed to the fact that a higher concentration of nucleation precursors promotes an increase in J .

3.6 FSA-Driven Nucleation Enhancement Mechanism

The clusters formed in the system via two main pathways: the pure SA-A pathway and SA-A-FSA pathways (Fig. 8). The pure SA-A nucleation pathway primarily formed stable (SA)₃·(A)₃ clusters through monomer addition and collision with SA·A cluster. ~~The SA-A-FSA nucleation pathway can be categorized into two routes.~~ The SA-A-FSA nucleation pathway can be categorized into two routes, with FSA acting as a “participator” in the SA-A-FSA-based nucleation process. This is in agreement with the results predicted by the molecular dynamics (MD) simulations. One route involved the initial formation of the stable cluster FSA·A, which then collided with one ~~SA molecule, an~~ FSA molecule, or another FSA·A cluster to form subsequent stable clusters and continue growing. The other route involved the initial formation of the stable (SA)₂·A cluster, which then collided with one FSA·A cluster to form the stable (SA)₂·(A)₂·FSA, continuing to grow through the addition of an A molecule ~~or an FSA molecule~~. Interestingly, at varying temperatures and concentrations of nucleating precursors, the FSA molecule exhibited distinct effects and contributions in the SA-A system. As the temperature increased, the contribution of the SA-A-FSA pathway rose from ~~516%~~ to ~~9792%~~ (Fig. 9(a)). Therefore, the cluster growth pathway involving FSA appears to prevail at relatively higher temperatures, such as during summer or at lower altitudes.

The involvement of FSA in the primary cluster formation pathway may also be influenced by the concentration of the precursors. Specifically, the contribution of the FSA participation pathway exhibited a negative correlation with [SA] or [A] at 278.15 K (Fig. 9(b-c)). Consequently, the contributions of the SA-A-FSA pathway may be more substantial in the clean atmospheric boundary layer with low [A] and [SA], such as in area distant from heavy traffic and emission sources of SA. Additionally, the contribution of the SA-A-FSA pathway increases as [FSA] rises (Fig. 9(d)). At ~~lower~~ [FSA] (10^4 - 10^3 molecules·cm⁻³), the contribution of SA-A-FSA pathway was only 35%, with cluster growth pathways predominantly governed by the formation of pure SA-A clusters. However, as [FSA] increased to 10^4 - 10^5 molecules·cm⁻³, the contribution of FSA-involving clusters rose to 84%, making the pathway involving FSA dominant for cluster formation in the SA-A-FSA system. Moreover, the SA-A-FSA mechanism contributed more significantly (97%) at higher [FSA] concentrations (10^5 - 10^6 - 10^7 molecules·cm⁻³). In summary, ~~consistent with the variation observed in R with temperature and precursor concentrations,~~ the contribution of the pathway involving FSA is significantly ~~prevalent~~ dominant in the NPF process with decreasing [SA] and [A] and increasing temperature and [FSA]. ~~These results suggest that FSA could be a significant contributor to SA-A atmospheric NPF, and the SA-A-FSA pathway may dominate in regions with high FSA emissions and relatively high temperatures. These results suggest that FSA could be a significant contributor to SA-A atmospheric NPF, and the SA-A-FSA pathway may prevail in regions with relatively higher temperatures and high FSA emissions, such as in Beijing, Shanghai, and Tangshan, where high concentrations of SO₃ and HCOOH are observed.~~

4. Summary and Conclusions

The potential contribution of FSA to gaseous and interfacial SO₃ hydrolysis, as well as its enhancement of atmospheric particle formation was investigated. Gaseous results indicated that SO₃ hydrolysis with FSA has a Gibbs free energy barrier as low as 1.5 kcal·mol⁻¹ and can effectively compete with SO₃ hydrolysis by HNO₃ (10^9 molecules·cm⁻³), HCOOH (10^8 molecules·cm⁻³) and H₂SO₄ (10^6 molecules·cm⁻³) over a temperature range of 280.0-320.0 K. Interfacial BOMD simulations illustrated that FSA-mediated SO₃ hydrolysis at the gas-liquid interface occurs through a stepwise mechanism and can be completed within a few picoseconds. ACDC kinetic simulations indicated that FSA significantly enhances cluster formation rates in the H₂SO₄-NH₃ system during

summer, increasing rates by more than 10^{5-10^7} times under conditions of high FSA concentrations and low H_2SO_4 and NH_3 levels. The H_2SO_4 - NH_3 -FSA nucleation mechanism exhibits a stronger nucleation ability than classical nucleation, making it a promising process for urban polluted environments rich in FSA sources. Meanwhile, the interfacial species formed, such as HSO_4^- , H_3O^+ and FSA^- , act to attract precursor species (e.g., H_2SO_4 , NH_3 and HNO_3) from the gas phase to the nanodroplet interface, thereby facilitating further particle growth. This study broadens our understanding of a novel SO_3 hydrolysis pathway involving FSA in polluted regions, identifies previously overlooked new particle formation (NPF) sources in industrial areas, and deepens knowledge of the atmospheric organic-sulfur cycle.

Data availability.

All data presented in this study are available upon request from the corresponding author.

Author contributions.

RW: methodology, investigation, funding acquisition, writing (original draft). RL: writing (review), data curation, methodology, investigation. SC: writing (review), data computation. RM: data curation, data computation. CZ: writing (editing), data curation, visualization, investigation. XM: data curation, project administration, writing (review and editing), funding acquisition. MK: methodology, writing (review and editing). TZ: writing (review and editing), funding acquisition.

Competing interests.

The authors declare that they have no known competing financial interests or personal relationships that could have appeared to influence the work reported in this paper.

Acknowledgments

This work was supported by the National Natural Science Foundation of China (No: ~~22073059~~; 22203052; ~~22073059~~; 42107109); the Key Cultivation Project of Shaanxi University of Technology (No: SLG2101); the Education Department of Shaanxi Provincial Government (No. 23JC023).

Declaration of competing interest

The authors declare that they have no known competing financial interests or personal relationships that could have appeared to influence the work reported in this paper.

Reference

- Abraham, M., Alekseenko, A., Basov, V., Bergh, C., Briand, E., Brown, A., Doijade, M., Fiorin, G., Fleischmann, S., Gorelov, S., Gouaillardet, G., Grey, A., Irrgang, M. E., Jalalypour, F., Jordan, J., Kutzner, C., Lemkul, J. A., Lundborg, M., Merz, P., Miletic, V., Morozov, D., Nabet, J., Pall, S., Pasquadibisceglie, A., Pellegrino, M., Santuz, H., Schulz, R., Shugaeva, T., Shvetsov, A., Villa, A., Wingermuehle, S., Hess, B., Lindahl, E. GROMACS 2024.3 Manual., <https://doi.org/10.5281/zenodo.13457083>, 2024.
- Bandyopadhyay, B., Kumar, P., and Biswas, P.: Ammonia catalyzed formation of sulfuric acid in troposphere: The curious case of a base promoting acid rain, *J. Phys. Chem. A*, 121, 3101-3108, <https://doi.org/10.1021/acs.jpca.7b01172>, 2017.
- Bao, J. L., Zhang, X., and Truhlar, D. G.: Barrierless association of CF₂ and dissociation of C₂F₄ by variational transition-state theory and system-specific quantum Rice-Ramsperger-Kassel theory, *Proc. Natl. Acad. Sci. U.S.A.*, 113, 13606-13611, <https://doi.org/10.1073/pnas.1616208113>, 2016.
- Becke, A. D.: Density-functional exchange-energy approximation with correct asymptotic behavior, *Phys. Rev. A*, 38, 3098-3100, <https://doi.org/10.1103/physreva.38.3098>, 1988.
- Berendsen, H. J. C., Postma, J. P. M., van Gunsteren, W. F., DiNola, A., and Haak, J. R.: Molecular dynamics with coupling to an external bath, *J. Chem. Phys.*, 81, 3684-3690, <https://doi.org/10.1063/1.448118>, 1984.
- Bondybey, V. E., and English, J. H.: Infrared spectra of SO₃ polymers and complexes in rare gas matrices, *J. Mol. Spectrosc.*, 109, 221-228, [https://doi.org/10.1016/0022-2852\(85\)90308-X](https://doi.org/10.1016/0022-2852(85)90308-X), 1985.
- Bussi, G., Donadio, D., and Parrinello, M.: Canonical sampling through velocity rescaling, *J. Chem. Phys.*, 126, 014101, <https://doi.org/10.1063/1.2408420>, 2007.
- Carmona-García, J., Trabelsi, T., Francés-Monerris, A., Cuevas, C. A., Saiz-Lopez, A., Roca-Sanjuán, D., and Francisco, J. S.: Photochemistry of HOSO₂ and SO₃ and implications for the production of sulfuric acid, *J. Am. Chem. Soc.*, 143, 18794-18802, <https://doi.org/10.1021/jacs.1c10153>, 2021.
- Chen, T., and Plummer, P. L.: Ab initio MO investigation of the gas-phase reaction sulfur trioxide + water. fwdarw. sulfuric acid, *J. Phys. Chem.*, 89, 3689-3693, <https://doi.org/10.1021/j100263a023>, 1985.
- Cheng, Y., Ding, C., Zhang, T., Wang, R., Mu, R., Li, Z., Li, R., Shi, J., and Zhu, C.: Barrierless reactions of C₂ Criegee intermediates with H₂SO₄ and their implication to oligomers and new particle formation, *J. Environ. Sci.*, 149, 574-584, <https://doi.org/10.1016/j.jes.2023.12.020>, 2025.
- Couling, S. B., Sully, K. J., and Horn, A. B.: Experimental study of the heterogeneous interaction of SO₃ and H₂O: formation of condensed phase molecular sulfuric acid hydrates, *J. Am. Chem. Soc.*, 125, 1994-2003, <https://doi.org/10.1021/ja0210704>, 2003.
- Ding, C., Wen, M. J., Zhang, T. L., Li, Z. Y., Li, R. R., Wang, R., Ou, T., Song, F. M. and Zhang, Q.: Molecular mechanisms and atmospheric implications of the simplest criegee intermediate and hydrochloric acid chemistry in the gas phase and at the aqueous interfaces, *Atmos. Environ.*, 330, 120558, <https://doi.org/10.1016/j.atmosenv.2024.120558>, 2024.
- Dong, Z., Francisco, J. S., and Long, B.: Ammonolysis of glyoxal at the air-water nanodroplet interface, *Angew. Chem. Int. Ed.*, 63, e202316060, <https://doi.org/10.1002/anie.202316060>, 2024.

- Fang, Y.-G., Wei, L., Francisco, J. S., Zhu, C., and Fang, W.-H.: Mechanistic insights into chloric acid production by hydrolysis of chlorine trioxide at an air-water interface, *J. Am. Chem. Soc.*, 146, 21052-21060, <https://doi.org/10.1021/jacs.4c06269>, 2024.
- Feng, Y., and Wang, C.: Surface Confinement of finite-size water droplets for SO₃ hydrolysis reaction revealed by molecular dynamics simulations based on a machine learning force field, *J. Am. Chem. Soc.*, 145, 10631-10640, <https://doi.org/10.1021/jacs.3c00698>, 2023.
- Fleig, D. G., Vainio, E., Andersson, K., Brink, A., Johnsson, F., and Hupa, M.: Evaluation of SO₃ measurement techniques in air and oxy-fuel combustion, *Energy Fuels*, 26, 5537-5549, <https://doi.org/10.1021/EF301127X>, 2012.
- Frisch, M. J., Trucks, G. W., Schlegel, H. B., Scuseria, G. E., Robb, M. A., Cheeseman, J. R., Scalmani, G., Barone, V., Mennucci, B., Petersson, G. A., Nakatsuji, H., Caricato, M., Li, X., Hratchian, H. P., Izmaylov, A. F., Bloino, J., Zheng, G., Sonnenberg, J. L., Hada, M., Ehara, M., Toyota, K., Fukuda, R., Hasegawa, J., Ishida, M., Nakajima, T., Honda, Y., Kitao, O., Nakai, H., Vreven, T., Montgomery, J. A., Jr., Peralta, J. E., Ogliaro, F., Bearpark, M., Heyd, J. J., Brothers, E., Kudin, K. N., Staroverov, V. N., Kobayashi, R., Normand, J., Raghavachari, K., Rendell, A., Burant, J. C., Iyengar, S. S., Tomasi, J., Cossi, M., Rega, N., Millam, J. M., Klene, M., Knox, J. E., Cross, J. B., Bakken, V., Adamo, C., Jaramillo, J., Gomperts, R., Stratmann, R. E., Yazyev, O., Austin, A. J., Cammi, R., Pomelli, C., Ochterski, J. W., Martin, R. L., Morokuma, K., Zakrzewski, V. G., Voth, G. A., Salvador, P., Dannenberg, J. J., Dapprich, S., Daniels, A. D., Farkas, Ö., Foresman, J. B., Ortiz, J. V., Cioslowski, J., and Fox, D. J.: Gaussian09 Revision D. 01, Gaussian Inc. Wallingford CT, <http://www.gaussian.com>, 2009.
- Gao, J., Wang, R., Zhang, T., Liu, F., and Wang, W.: Effect of methyl hydrogen sulfate on the formation of sulfuric acid-ammonia clusters: A theoretical study, *J. Chin. Chem. Soc.*, 70, 689-698, <https://doi.org/10.1002/jccs.202200148>, 2023.
- Gao, Q., Dong, Z., and Long, B.: Reactions of sulfur trioxide with hypochlorous acid catalyzed by water in gas phase and at the air-water nanodroplet interface in the atmosphere: An important sink for hypochlorous acid, *Atmospheric Environ.*, 331, 120574, <https://doi.org/10.1016/j.atmosenv.2024.120574>, 2024.
- Glowacki, D. R., Liang, C. H., Morley, C., Pilling, M. J., and Robertson, S. H.: MESMER: an open-source master equation solver for multi-energy well reactions, *J. Phys. Chem. A*, 116, 9545-9560, <https://doi.org/10.1021/jp3051033>, 2012.
- Goedecker, S., Teter, M., and Hutter, J.: Separable dual-space Gaussian pseudopotentials, *Phys. Rev. B*, 54, 1703, <https://doi.org/10.1103/PhysRevB.54.1703>, 1996.
- Grimme, S., Antony, J., Ehrlich, S., and Krieg, H.: A consistent and accurate ab initio parametrization of density functional dispersion correction (DFT-D) for the 94 elements H-Pu, *J. Chem. Phys.*, 132, 154104, <https://doi.org/10.1063/1.3382344>, 2010.
- Hess, B., Bekker, H., Berendsen, H. J. C., and Fraaije, J. G. E. M.: LINCS: A linear constraint solver for molecular simulations, *J. Comput. Chem.*, 18, 1463-1472, [https://doi.org/10.1002/\(SICI\)1096-987X\(199709\)18:12<1463::AID-JCC4>3.0.CO;2-H](https://doi.org/10.1002/(SICI)1096-987X(199709)18:12<1463::AID-JCC4>3.0.CO;2-H), 1997.
- Hutter, J., Iannuzzi, M., Schiffmann, F., and VandeVondele, J.: cp2k: atomistic simulations of condensed matter systems, *Wiley Interdiscip. Rev. Comput. Mol. Sci.*, 4, 15-25, <https://doi.org/10.1002/wcms.1159>, 2014.

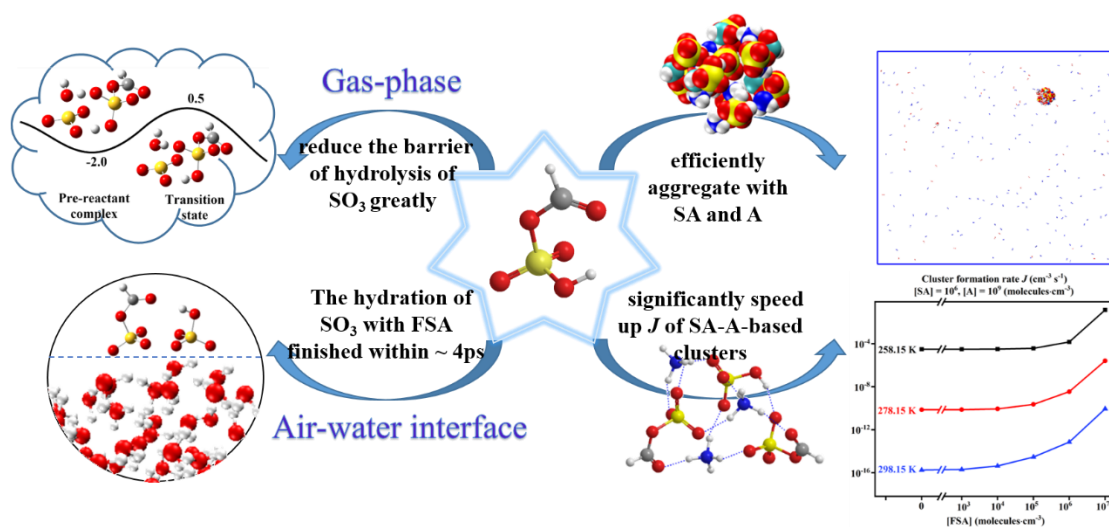
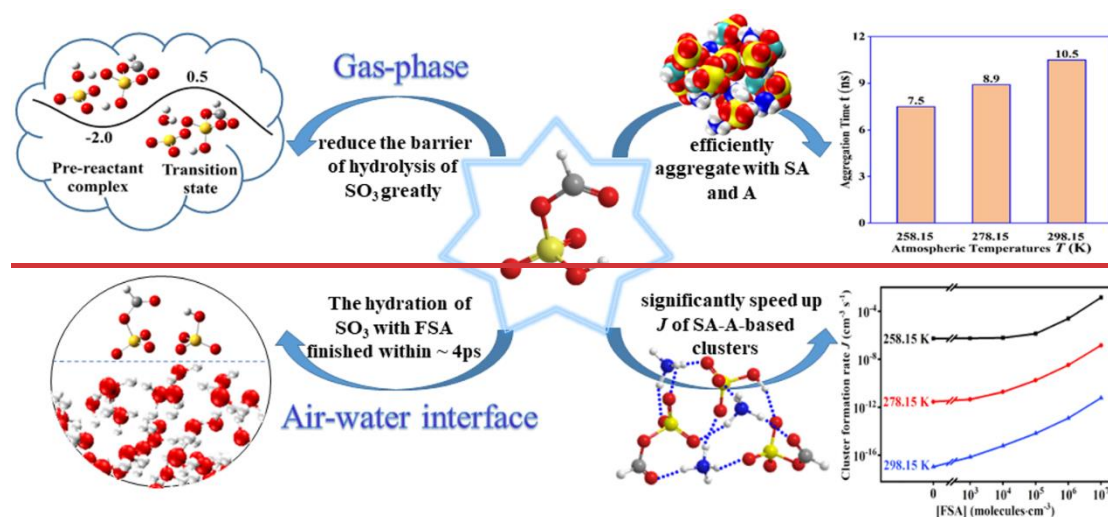
- Kangas, P., Hänninen, V., and Halonen, L.: An ab initio molecular dynamics study of the hydrolysis reaction of sulfur trioxide catalyzed by a formic acid or water molecule, *J. Phys. Chem. A*, 124, 1922-1928, <https://doi.org/10.1021/acs.jpca.9b11954>, 2020.
- Kumar, A., Mallick, S., and Kumar, P.: Oxidation of HOSO^\cdot by Cl^\cdot : a new source of SO_2 in the atmosphere?, *Phys. Chem. Chem. Phys.*, 23, 18707-18711, <https://doi.org/10.1039/D1CP01048D>, 2021..
- Kumar, A., Iyer, S., Barua, S., Brean, J., Besic, E., Seal, P., Dall'Osto, M., Beddows, D. C. S., Sarnela, N., Jokinen, T., Sipilä, M., Harrison, R. M., and Rissanen, M.: Direct measurements of covalently bonded sulfuric anhydrides from gas-phase reactions of SO_3 with acids under ambient conditions, *J. Am. Chem. Soc.*, 146, 15562-15575, <https://doi.org/10.1021/jacs.4c04531>, 2024.
- Lee, C., Yang, W., and Parr, R. G.: Development of the Colle-Salvetti correlation-energy formula into a functional of the electron density, *Phys. Rev. B*, 37, 785-789, <https://doi.org/10.1103/PHYSREVB.37.785>, 1988.
- Li, H., Zhong, J., Vehkamäki, H., Kurtén, T., Wang, W., Ge, M., Zhang, S., Li, Z., Zhang, X., Francisco, J. S., and Zeng, X. C.: Self-Catalytic reaction of SO_3 and NH_3 to produce sulfamic acid and its implication to atmospheric particle formation, *J. Am. Chem. Soc.*, 140, 11020-11028, <https://doi.org/10.1021/jacs.8b04928>, 2018.
- Li, L., Zhang, Q. Z., Wei, Y. Y., Wang, Q. and Wang, W. X.: Theoretical Study on the Gas-Phase and Aqueous Interface Reaction Mechanism of Criegee Intermediates with 2-Methylglyceric Acid and the Nucleation of Products. *Int. J. Mol. Sci.* 24, 5400, <https://doi.org/10.3390/ijms24065400>, 2023.
- Li, M., Li, L., Liu, S., Zhang, Q., Wang, W., and Wang, Q.: Insights into the catalytic effect of atmospheric organic trace species on the hydration of Criegee intermediates, *Sci. Total. Environ.*, 949, 174877, <https://doi.org/10.1016/j.scitotenv.2024.174877>, 2024a.
- Li, M., Zhang, Y., Yu, X., Li, L., Wang, S., Zhang, Q., Wang, W., and Wang, Q.: Mechanistic insights into Criegee intermediates with benzoic acid at gas-phase and air-water interface and nucleation of product, *Atmospheric Environ.*, 320, 120338, <https://doi.org/10.1016/j.atmosenv.2024.120338>, 2024b.
- Liu, J., Liu, L., Rong, H., and Zhang, X.: The potential mechanism of atmospheric new particle formation involving amino acids with multiple functional groups, *Phys. Chem. Chem. Phys.*, 23, 10184-10195, <https://doi.org/10.1039/D0CP06472F>, 2021a.
- Liu, L., Zhong, J., Vehkamäki, H., Kurtén, T., Du, L., Zhang, X., Francisco, J. S., and Zeng, X. C.: Unexpected quenching effect on new particle formation from the atmospheric reaction of methanol with SO_3 , *Proc. Natl. Acad. Sci. U.S.A.*, 116, 24966-24971, <https://doi.org/10.1073/pnas.1915459116>, 2019.
- Liu, L., Yu, F., Tu, K., Yang, Z., and Zhang, X.: Influence of atmospheric conditions on the role of trifluoroacetic acid in atmospheric sulfuric acid-dimethylamine nucleation, *Atmos. Chem. Phys.*, 21, 6221-6230, <https://doi.org/10.5194/acp-21-6221-2021>, 2021b.
- Long, B., Long, Z. W., Wang, Y. B., Tan, X. F., Han, Y. H., Long, C. Y., Qin, S. J., and Zhang, W. J.: Formic acid catalyzed gas-phase reaction of H_2O with SO_3 and the reverse reaction: A theoretical study, *ChemPhysChem*, 13, 323-329, <https://doi.org/10.1002/cphc.201100558>, 2012.

- Long, B., Chang, C.-R., Long, Z.-W., Wang, Y.-B., Tan, X.-F., and Zhang, W.-J.: Nitric acid catalyzed hydrolysis of SO₃ in the formation of sulfuric acid: A theoretical study, *Chem. Phys. Lett.*, 581, 26-29, <https://doi.org/10.1016/j.cplett.2013.07.012>, 2013.
- Long, B., Xia, Y., Bao, J. L., Carmona-García, J., Gómez Martín, J. C., Plane, J. M. C., Saiz-Lopez, A., Roca-Sanjuán, D., and Francisco, J. S.: Reaction of SO₃ with HONO₂ and implications for sulfur partitioning in the atmosphere, *J. Am. Chem. Soc.*, 144, 9172-9177, <https://doi.org/10.1021/jacs.2c03499>, 2022.
- Lu, T., and Chen, F.: Multiwfn: A multifunctional wavefunction analyzer, *J. Comput. Chem.*, 33, 580-592, <https://doi.org/10.1002/jcc.22885>, 2012.
- Lu, T.: Sobtop, Version 1.0, <http://sobereva.com/soft/Sobtop/>, 2023.
- Lv, G., Sun, X., Zhang, C., and Li, M.: Understanding the catalytic role of oxalic acid in SO₃ hydration to form H₂SO₄ in the atmosphere, *Atmos. Chem. Phys.*, 19, 2833-2844, <https://doi.org/10.5194/acp-19-2833-2019>, 2019.
- Ma, X., Zhao, X., Huang, Z., Wang, J., Lv, G., Xu, F., Zhang, Q., and Wang, W.: Determination of reactions between Criegee intermediates and methanesulfonic acid at the air-water interface, *Sci. Tot. Environ.*, 707, 135804, <https://doi.org/10.1016/j.scitotenv.2019.135804>, 2020.
- Mackenzie, R. B., Dewberry, C. T., and Leopold, K. R.: Gas phase observation and microwave spectroscopic characterization of formic sulfuric anhydride, *Science*, 349, 58-61, <https://doi.org/10.1126/science.aaa9704>, 2015.
- Mardirossian N. and Head-Gordon M.: How Accurate Are the Minnesota Density Functionals for Noncovalent Interactions, Isomerization Energies, Thermochemistry, and Barrier Heights Involving Molecules Composed of Main-Group Elements, *J. Chem. Theory Comput.*, 12, 4303-4325, <https://doi.org/10.1021/acs.jctc.6b00637>, 2016.
- Martínez, L., Andrade, R., Birgin, E. G., and Martínez, J. M.: PACKMOL: A package for building initial configurations for molecular dynamics simulations, *J. Comput. Chem.*, 30, 2157-2164, <https://doi.org/10.1002/jcc.21224>, 2009.
- Martins-Costa, M. T., and Ruiz-López, M. F.: The structure of carbon dioxide at the air-water interface and its chemical implications, *Chem. Eur. J.* 30, e202400825, <https://doi.org/10.1002/chem.202400825>, 2024.
- McGrath, M. J., Olenius, T., Ortega, I. K., Loukonen, V., Paasonen, P., Kurtén, T., Kulmala, M., and Vehkamäki, H.: Atmospheric Cluster Dynamics Code: a flexible method for solution of the birth-death equations, *Atmos. Chem. Phys.*, 12, 2345-2355, <https://doi.org/10.5194/acp-12-2345-2012>, 2012.
- Meana-Pañeda, R., Zheng, J., Bao, J. L., Zhang, S., Lynch, B. J., Corchado, J. C., Chuang, Y.-Y., Fast, P. L., Hu, W.-P., Liu, Y.-P., Lynch, G. C., Nguyen, K. A., Jackels, C. F., Fernández-Ramos, A., Ellingson, B. A., Melissas, V. S., Villà, J., Rossi, I., Coitiño, E. L., Pu, J., Albu, T. V., Zhang, R. M., Xu, X., Ratkiewicz, A., Steckler, R., Garrett, B. C., Isaacson, A. D., and Truhlar, D. G.: Polyrate 2023: A computer program for the calculation of chemical reaction rates for polyatomics. New version announcement, *Comput. Phys. Commun.*, 294, 108933, <https://doi.org/10.1016/j.cpc.2023.108933>, 2024.
- Morokuma, K., and Muguruma, C.: Ab initio molecular orbital study of the mechanism of the gas phase reaction SO₃ + H₂O: Importance of the second water molecule, *J. Am. Chem. Soc.*, 116, 10316-10317, <https://doi.org/10.1021/JA00101A068>, 1994.

- Neese, F.: The ORCA program system, WIREs Comput. Mol. Sci., 2, 73-78, <https://doi.org/10.1002/wcms.81>, 2012.
- Partanen, L., Vehkamäki, H., Hansen, K., Elm, J., Henschel, H., Kurtén, T., Halonen, R., and Zapadinsky, E.: Effect of conformers on free energies of atmospheric complexes, J. Phys. Chem. A, 120, 8613-8624, <https://doi.org/10.1021/acs.jpca.6b04452>, 2016.
- Pereira A. T., Ribeiro A. J. M., Fernandes P. A. and Ramos M. J.: Benchmarking of density functionals for the kinetics and thermodynamics of the hydrolysis of glycosidic bonds catalyzed by glycosidases, Int. J. Quantum Chem., 117, e254092017, <https://doi.org/10.1002/qua.25409>, 2017.
- Phillips, J. C., Braun, R., Wang, W., Gumbart, J., Tajkhorshid, E., Villa, E., Chipot, C., Skeel, R. D., Kalé, L., and Schulten, K.: Scalable molecular dynamics with NAMD, J. Comput. Chem., 26, 1781-1802, <https://doi.org/10.1002/jcc.20289>, 2005.
- Reiner, T., and Arnold, F.: Laboratory flow reactor measurements of the reaction $\text{SO}_3 + \text{H}_2\text{O} + \text{M} \rightarrow \text{H}_2\text{SO}_4 + \text{M}$: Implications for gaseous H_2SO_4 and aerosol formation in the plumes of jet aircraft, J. Geophys. Res., 20, 2659-2662, <https://doi.org/10.1029/93GL02996>, 1993.
- Rong, H., Liu, L., Liu, J., and Zhang, X.: Glyoxylic sulfuric anhydride from the gas-phase reaction between glyoxylic acid and SO_3 : A potential nucleation precursor, J. Phys. Chem. A, 124, 3261-3268, <https://doi.org/10.1021/acs.jpca.0c01558>, 2020.
- Sarkar, S., Oram, B. K., and Bandyopadhyay, B.: Influence of ammonia and water on the fate of sulfur trioxide in the troposphere: Theoretical investigation of sulfamic acid and sulfuric acid formation pathways, J. Phys. Chem. A, 123, 3131-3141, <https://doi.org/10.1021/acs.jpca.8b09306>, 2019.
- Smith, C. J., Huff, A. K., Ward, R. M., and Leopold, K. R.: Carboxylic sulfuric anhydrides, J. Phys. Chem. A, 124, 601-612, <https://doi.org/10.1126/science.1180315>, 2020.
- Smith, C. J., Huff, A. K., Ward, R. M. and Leopold, K. R.: Carboxylic sulfuric anhydrides, J. Phys. Chem. A, 124, 601-612, <https://doi.org/10.1021/acs.jpca.9b09310>, 2020.
- Sun, G., Li, H., Hou, J., Wang, H., Wang, J., Lu, Z., and Gao, X.: Molecular behavior of ethylene glycol/1,2-Butanediol Mixtures at the vapor-liquid interface, Ind. Eng. Chem. Res., 63, 4853-4865, <https://doi.org/10.1021/acs.iecr.3c03410>, 2024.
- Tan, S., Zhang, X., Lian, Y., Chen, X., Yin, S., Du, L., and Ge, M.: OH group orientation leads to organosulfate formation at the liquid aerosol surface, J. Am. Chem. Soc., 144, 16953-16964, <https://doi.org/10.1021/jacs.2c05807>, 2022.
- Tang, B., Bai, Q., Fang, Y.-G., Francisco, J. S., Zhu, C., and Fang, W.-H.: Mechanistic insights into N_2O_5 -Halide ions chemistry at the air-water interface, J. Am. Chem. Soc., 146, 21742-21751, <https://doi.org/10.1021/jacs.4c05850>, 2024.
- Tao, E. L., Li, J. Y., Soriano, S., and Tao, F.-M. J. C. J. o. C. P.: Quantum chemical study of potential energy surface in the formation of atmospheric sulfuric acid, Chin. J. Chem. Phys. 31, 503-509, <https://doi.org/10.1063/1674-0068/31/cjcp1805126>, 2018.
- Tchinda N. T., Du L, Liu L and Zhang X. H.: Pyruvic acid, an efficient catalyst in SO_3 hydrolysis and effective clustering agent in sulfuric-acid-based new particle formation, Atmos. Chem. Phys., 22, 1951-1963, <https://doi.org/10.5194/acp-22-1951-2022>, 2022.
- Torrent-Sucarrat, M., Francisco, J. S., and Anglada, J. M.: Sulfuric acid as autocatalyst in the formation of sulfuric acid, J. Am. Chem. Soc., 134, 20632-20644, <https://doi.org/10.1021/ja307523b>, 2012.

- Venkataraman, C., Mehra, A., and Mhaskar, P.: Mechanisms of sulphate aerosol production in clouds: effect of cloud characteristics and season in the Indian region, *Tellus B*, 53, 260-272, <https://doi.org/10.3402/tellusb.v53i3.16595>, 2001.
- Wan, Z., Zhu, C., and Francisco, J. S.: Molecular insights into the spontaneous generation of Cl_2O in the reaction of ClONO_2 and HOCl at the air-water interface, *J. Am. Chem. Soc.*, 145, 17478-17484, <https://doi.org/10.1021/jacs.3c06527>, 2023.
- Wang, R., Cheng, Y., Chen, S., Li, R., Hu, Y., Guo, X., Zhang, T., Song, F., and Li, H.: Reaction of SO_3 with H_2SO_4 and its implications for aerosol particle formation in the gas phase and at the air-water interface, *Atmos. Chem. Phys.*, 24, 4029-4046, <https://doi.org/10.5194/acp-24-4029-2024>, 2024.
- Wei, Y. Y., Zhang, Q. Z., Huo, X. X., Wang, W. X and Wang, Q.: The reaction of Criegee intermediates with formamide and its implication to atmospheric aerosols, *Chemosphere*, 296, 133717, <https://doi.org/10.1016/j.chemosphere.2022.133717>, 2022.
- Yang, Y., Liu, L., Wang, H., and Zhang, X.: Molecular-Scale mechanism of sequential reaction of oxalic acid with SO_3 : Potential participator in atmospheric aerosol nucleation, *J. Phys. Chem. A*, 125, 4200-4208, <https://doi.org/10.1021/acs.jpca.1c02113>, 2021.
- Yao, L., Garmash, O., Bianchi, F., Zheng, J., Yan, C., Kontkanen, J., Junninen, H., Mazon, S. B., Ehn, M., Paasonen, P., Sipilä, M., Wang, M., Wang, X., Xiao, S., Chen, H., Lu, Y., Zhang, B., Wang, D., Fu, Q., Geng, F.-H., Li, L., Wang, H., Qiao, L., Yang, X., Chen, J., Kerminen, V.-M., Petäjä, T., Worsnop, D. R., Kulmala, M., and Wang, L. J. S.: Atmospheric new particle formation from sulfuric acid and amines in a Chinese megacity, *Science*, 361, 278-281, <https://doi.org/10.1126/science.aao4839>, 2018.
- York, D. M., Darden, T. A., and Pedersen, L. G.: The effect of long-range electrostatic interactions in simulations of macromolecular crystals: A comparison of the Ewald and truncated list methods, *J. Chem. Phys.*, 99, 8345-8348, <https://doi.org/10.1063/1.465608>, 1993.
- Zhang, H., Kupiainen-Määttä, O., Zhang, X., Molinero, V., Zhang, Y., and Li, Z.: The enhancement mechanism of glycolic acid on the formation of atmospheric sulfuric acid-ammonia molecular clusters, *J. Chem. Phys.*, 146, 184308, <https://doi.org/10.1063/1.4982929>, 2017.
- Zhang, H., Wang, W., Pi, S., Liu, L., Li, H., Chen, Y., Zhang, Y., Zhang, X., and Li, Z.: Gas phase transformation from organic acid to organic sulfuric anhydride: Possibility and atmospheric fate in the initial new particle formation, *Chemosphere*, 212, 504-512, <https://doi.org/10.1016/j.chemosphere.2018.08.074>, 2018.
- Zhang, H., Wang, W., Fan, L., Li, J., Ren, Y., Li, H., Gao, R., and Xu, Y.: The role of sulfur cycle in new particle formation: Cycloaddition reaction of SO_3 to H_2S , *J. Environ. Sci.*, 148, 489-501, <https://doi.org/10.1016/j.jes.2023.09.010>, 2025.
- Zhang, J., and Dolg, M.: ABCcluster: the artificial bee colony algorithm for cluster global optimization, *Phys. Chem. Chem. Phys.*, 17, 24173-24181, <https://doi.org/10.1039/C5CP04060D>, 2015.
- Zhang, Z., Yin, H., Shang, Y., and Luo, S.-N.: Accurate rate constants for barrierless dissociation of ethanol: VRC-VTST and SS-QRRK calculations with the cheaper DFT method, *Chem. Phys. Lett.*, 823, 140522, <https://doi.org/10.1016/j.cplett.2023.140522>, 2023.
- Zhang, Z. P., Wang, S. H., Shang, Y. L., Liu, J. H., and Luo, S. N.: Theoretical study on ethylamine dissociation reactions using VRC-VTST and SS-QRRK methods, *J. Phys. Chem. A*, 128, 2191-2199, <https://doi.org/10.1021/acs.jpca.3c08373>, 2024.

766 Zhao, Z., Kong, K., Wang, S., Zhou, Y., Cheng, D., Wang, W., Zeng, X. C., and Li, H. J. T. J. o. P.
 767 C. L.: Understanding hygroscopic nucleation of sulfate aerosols: combination of molecular
 768 dynamics simulation with classical nucleation theory, *J. Phys. Chem. Lett.*, 10, 1126-1132,
 769 <https://doi.org/10.1021/acs.jpcllett.9b00152>, 2019.
 770 Zhong, J., Zhu, C., Li, L., Richmond, G. L., Francisco, J. S., and Zeng, X. C.: Interaction of SO₂
 771 with the surface of a water nanodroplet, *J. Am. Chem. Soc.*, 139, 17168-17174,
 772 <https://doi.org/10.1021/jacs.7b09900>, 2017.
 773 Zhong, J., Li, H., Kumar, M., Liu, J., Liu, L., Zhang, X., Zeng, X. C., and Francisco, J. S.:
 774 Mechanistic insight into the reaction of organic acids with SO₃ at the air-water interface, 58,
 775 8351-8355, <https://doi.org/10.1002/anie.201900534>, 2019.



Graphic Abstract

Figure Captions

Fig. 1. Energy diagrams for SO_3 hydrolysis with FSA at the CCSD(T)-F12/cc-pVDZ-F12//M06-2X/6-311++G(2d~~df~~,2pd~~pd~~) level.

Fig. 2. BOMD simulations of $\text{HSO}_4^- \cdots \text{FSA} \cdots \text{H}_3\text{O}^+$ ion pair formation from SO_3 hydrolysis with FSA at the air-water interface. (Top: Snapshot structures from BOMD simulations, showing the ion pair formation. Bottom: Time evolution of key bond distances S-O1, O5-H3, and O1-H2 during the induced mechanism.)

Fig. 3. ESP-mapped vdW surfaces of sulfuric acid (SA), ammonia (A) and formic sulfuric anhydride (FSA). Blue, red, yellow, cyan, and white spheres represent N, O, S, C, and H atoms, respectively, with ESP in $\text{kcal} \cdot \text{mol}^{-1}$.

Fig. 4. ~~(a) Bar graph of aggregation completion time at different atmospheric temperatures; (b) snapshots-Snapshots~~ of nucleation simulation at 258.15 K from FSA, SA and A using the VDW representation, with N_2 and O_2 shown using the line drawing method.

Fig. 5. Histogram of (a) Gibbs free energy of formation (ΔG , $\text{kcal} \cdot \text{mol}^{-1}$) and (b) evaporation rate coefficient (γ , s^{-1}) for key pure SA-A clusters and FSA-containing stable clusters at 258.15, 278.15 and 298.15 K.

Fig. 6. ~~(a) Cluster formation rate (J , $\text{cm}^{-3} \cdot \text{s}^{-1}$) and (b) enhancement factor R with $[\text{SA}] = 10^6$ molecules $\cdot \text{cm}^{-3}$, $[\text{A}] = 10^9$ molecules $\cdot \text{cm}^{-3}$ at three temperatures (black: 258.15 K, red: 278.15 K, blue: 298.15 K). Cluster formation rate (J , $\text{cm}^{-3} \cdot \text{s}^{-1}$) with $[\text{SA}] = 10^6$ molecules $\cdot \text{cm}^{-3}$, $[\text{A}] = 10^9$ molecules $\cdot \text{cm}^{-3}$ at three temperatures (black: 258.15 K, red: 278.15 K, blue: 298.15 K).~~

Fig. 7. ~~(a) The cluster formation rate (J , $\text{cm}^{-3} \cdot \text{s}^{-1}$) and (b) enhancement factor R as a function of $[\text{A}]$ with $[\text{FSA}] = 10^6$ molecules $\cdot \text{cm}^{-3}$ at 278.15 K for five $[\text{SA}]$ levels (black: 10^4 , red: 10^5 , blue: 10^6 , green: 10^7 , purple: 10^8 molecules $\cdot \text{cm}^{-3}$). The cluster formation rate (J , $\text{cm}^{-3} \cdot \text{s}^{-1}$) as a function of (a) $[\text{SA}]$ and (b) $[\text{A}]$, with different concentrations of $[\text{FSA}] = 10^3$ - 10^7 molecules $\cdot \text{cm}^{-3}$ at 278.15 K.~~

Fig. 8. Primary growth pathways of clusters at $T = 278.15$ K, $[\text{SA}] = 10^6$ molecules $\cdot \text{cm}^{-3}$, $[\text{A}] = 10^9$ molecules $\cdot \text{cm}^{-3}$, and $[\text{FSA}] = 10^3$ - 10^7 molecules $\cdot \text{cm}^{-3}$. Blue and orange arrows represent the SA-A-based and SA-A-FSA-based pathways, respectively.

Fig. 9. Influence of (a) temperature, (b) $[\text{SA}]$, (c) $[\text{A}]$ and (d) $[\text{FSA}]$ on the relative contribution of the pure SA-A pathway and the FSA-containing pathway to the flux out of the system.

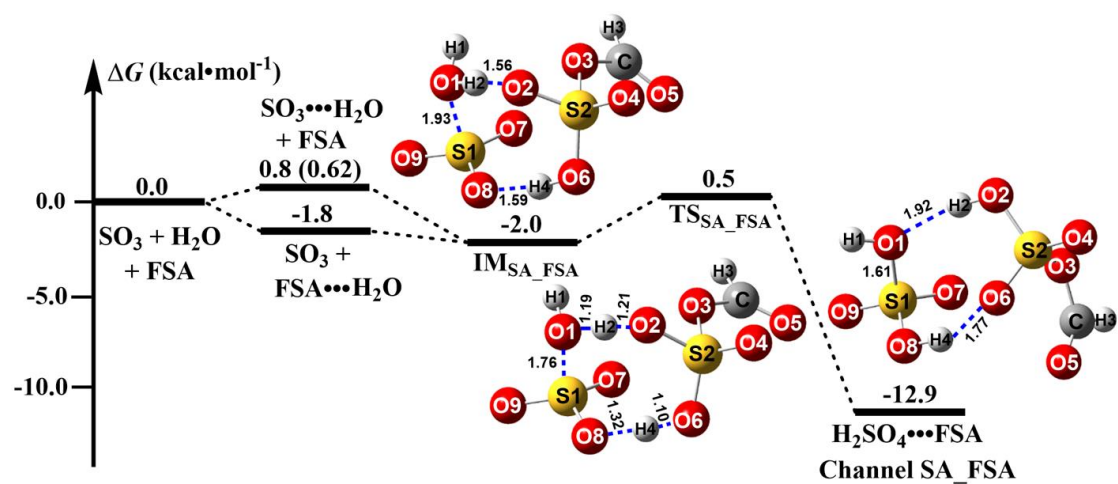


Fig. 1. Energy diagrams for SO_3 hydrolysis with FSA at the CCSD(T)-F12/cc-pVDZ-F12//M06-2X/6-311++G(2d~~df~~,2p~~dp~~) level.

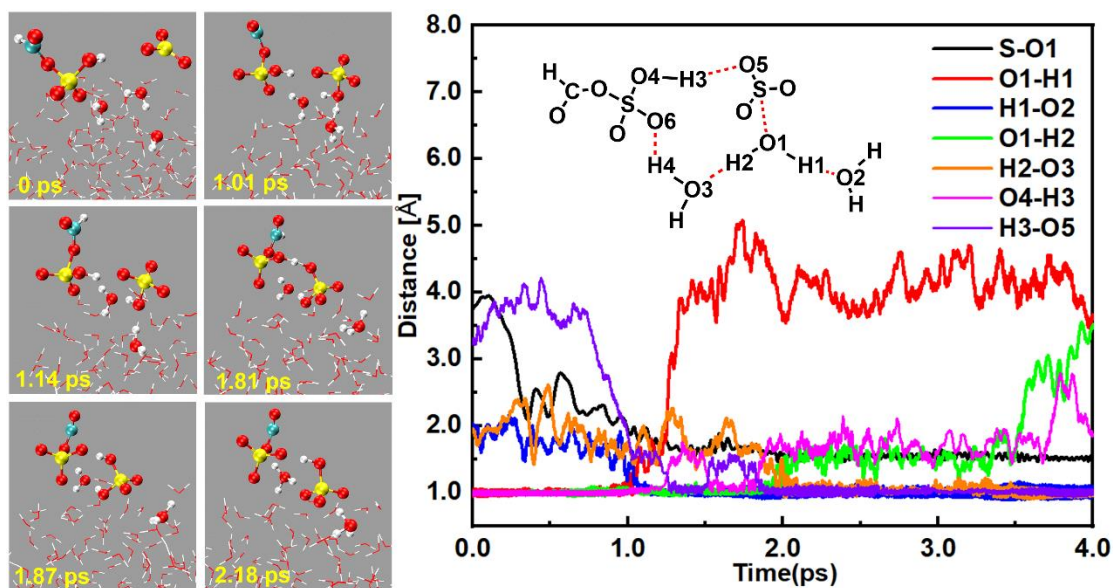
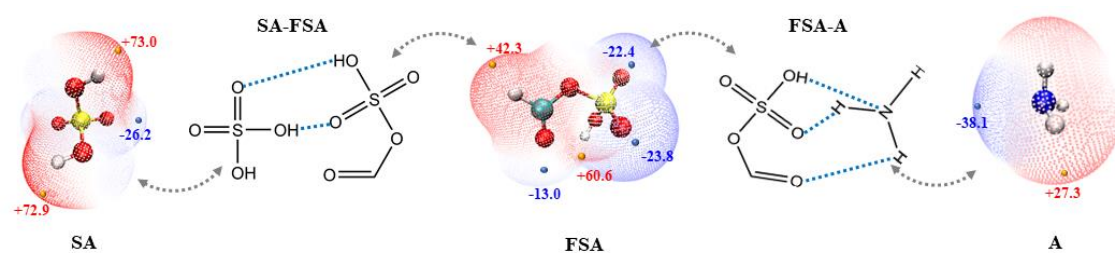


Fig. 2. BOMD simulations of $\text{HSO}_4^- \cdots \text{FSA}^- \cdots \text{H}_3\text{O}^+$ ion pair formation from SO_3 hydrolysis with FSA at the air-water interface. (Top: Snapshot structures from BOMD simulations, showing the ion pair formation. Bottom: Time evolution of key bond distances S-O1, O5-H3, and O1-H2 during the induced mechanism.)

816

817



818 **Fig. 3.** ESP-mapped vdW surfaces of sulfuric acid (SA), ammonia (A) and formic sulfuric anhydride
 819 (FSA). Blue, red, yellow, cyan, and white spheres represent N, O, S, C, and H atoms, respectively,
 820 with ESP in kcal·mol⁻¹.

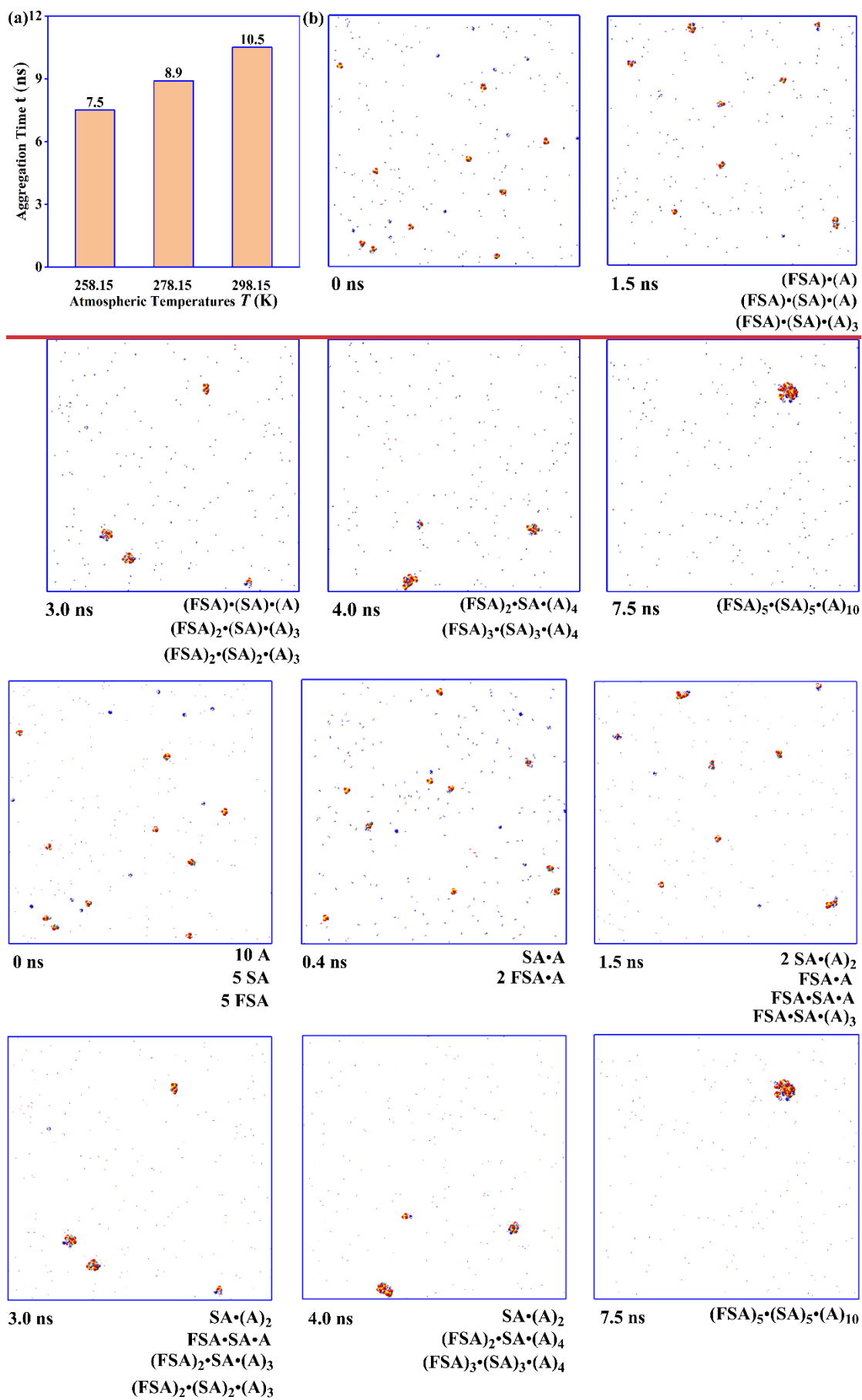


Fig. 4. (a) Bar graph of aggregation completion time at different atmospheric temperatures; (b) snapshots of nucleation simulation at 258.15 K from FSA, SA and A using the VDW representation, with N₂ and O₂ shown using the line drawing method. **Fig. 4.** Snapshots of nucleation simulation at 258.15 K from FSA, SA and A using the vdW representation, with N₂ and O₂ shown using the line drawing method.

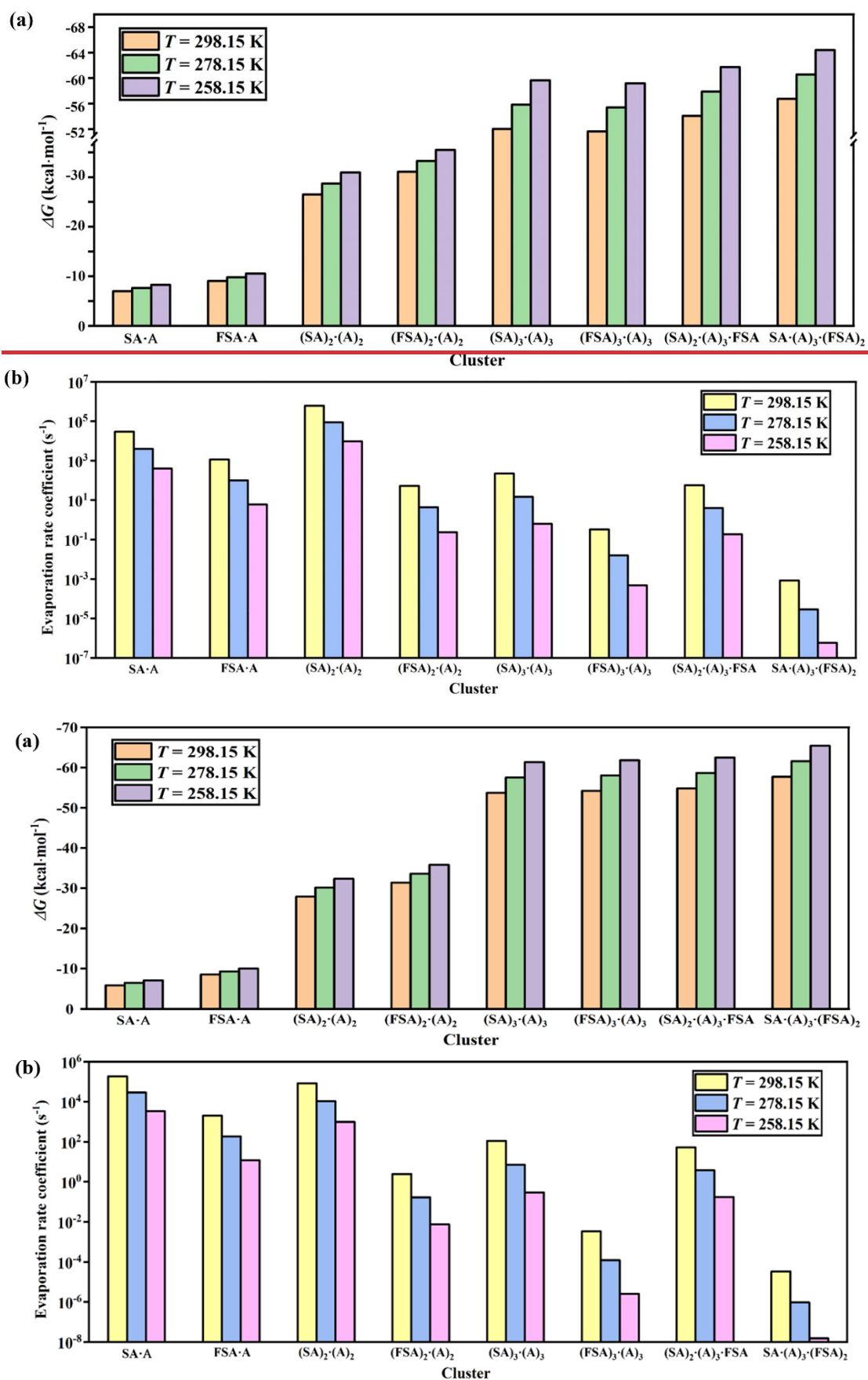


Fig. 5. Histogram of (a) Gibbs free energy of formation (ΔG , kcal·mol⁻¹) and (b) evaporation rate

831 coefficient (γ , s⁻¹) for key pure SA-A clusters and FSA-containing stable clusters at 258.15, 278.15
832 and 298.15 K.

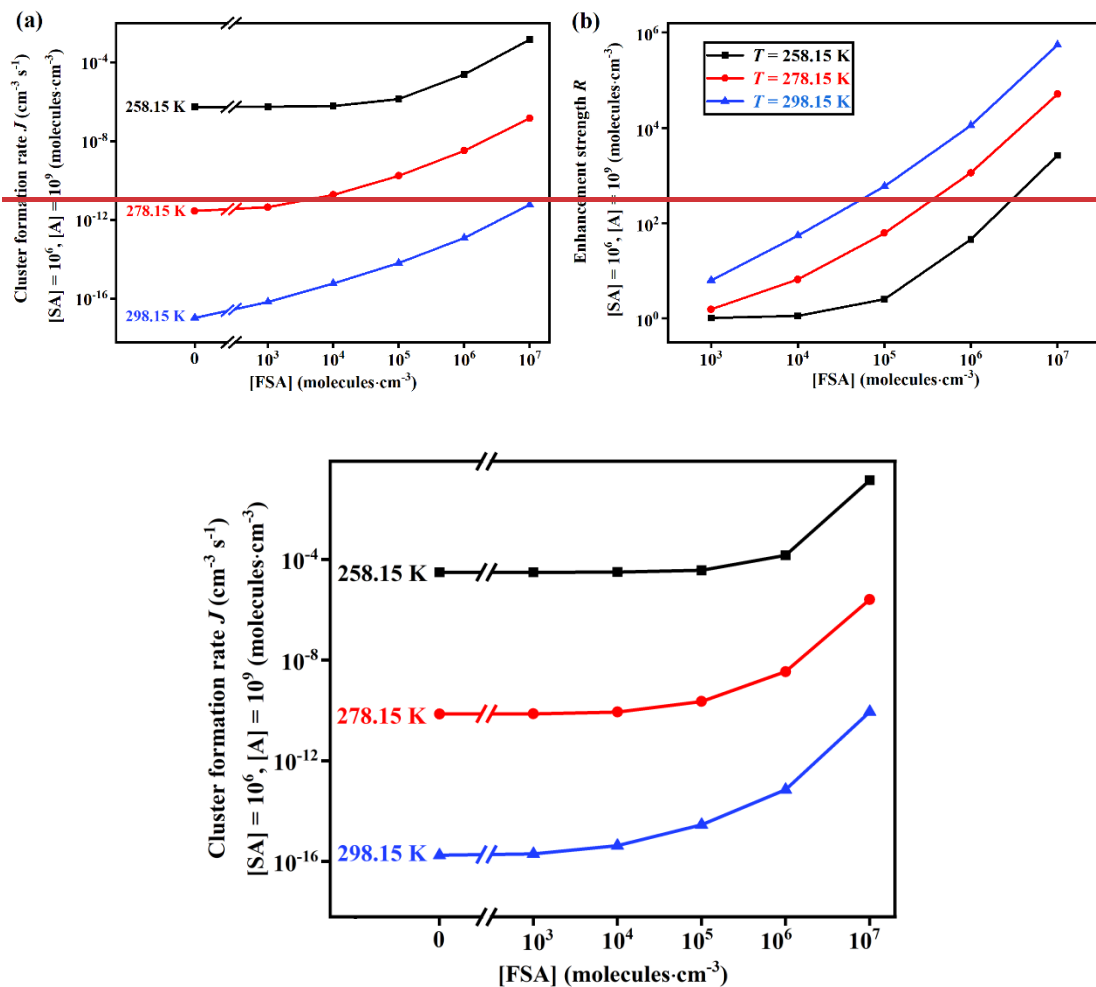


Fig. 6. Cluster formation rate (J , $\text{cm}^{-3} \text{s}^{-1}$) with $[\text{SA}] = 10^6 \text{ molecules} \cdot \text{cm}^{-3}$, $[\text{A}] = 10^9 \text{ molecules} \cdot \text{cm}^{-3}$ at three temperatures (black: 258.15 K, red: 278.15 K, blue: 298.15 K). **Fig. 6.** (a) Cluster formation rate (J , $\text{cm}^{-3} \text{s}^{-1}$) and (b) enhancement factor R with $[\text{SA}] = 10^6 \text{ molecules} \cdot \text{cm}^{-3}$, $[\text{A}] = 10^9 \text{ molecules} \cdot \text{cm}^{-3}$ at three temperatures (black: 258.15 K, red: 278.15 K, blue: 298.15 K).

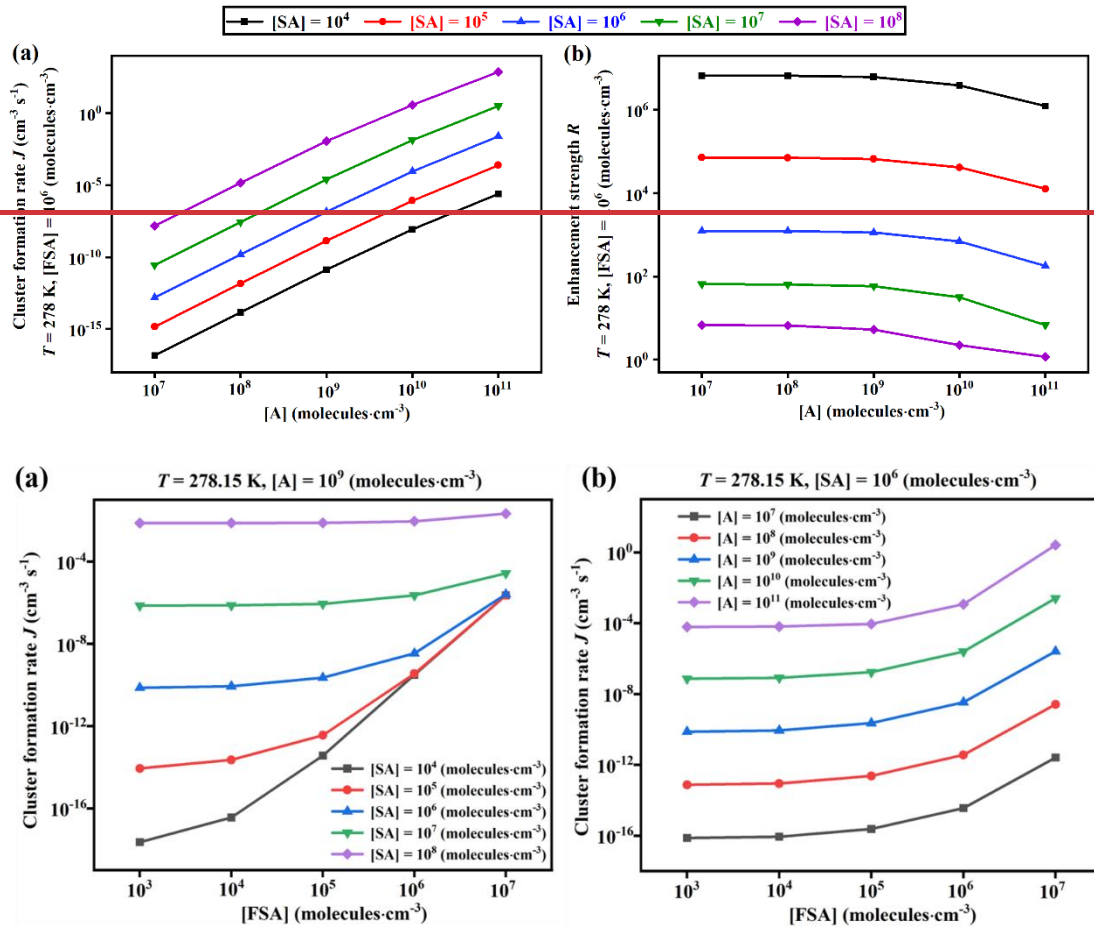


Fig. 7. The cluster formation rate (J , $\text{cm}^{-3}\cdot\text{s}^{-1}$) as a function of (a) $[SA]$ and (b) $[A]$, with different concentrations of $[FSA] = 10^3$ - $10^7 \text{ molecules}\cdot\text{cm}^{-3}$ at 278.15 K. **Fig. 7.** (a) The cluster formation rate (J , $\text{cm}^{-3}\cdot\text{s}^{-1}$) and (b) enhancement factor R as a function of $[A]$ with $[FSA] = 10^6 \text{ molecules}\cdot\text{cm}^{-3}$ at 278.15 K for five $[SA]$ levels (black: 10^4 , red: 10^5 , blue: 10^6 , green: 10^7 , purple: $10^8 \text{ molecules}\cdot\text{cm}^{-3}$).

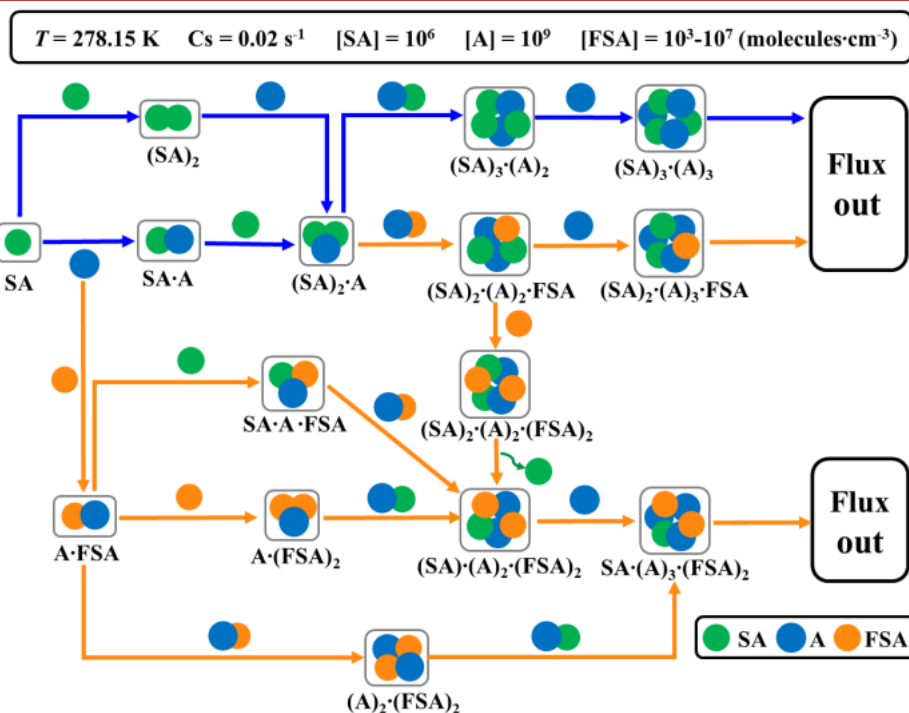
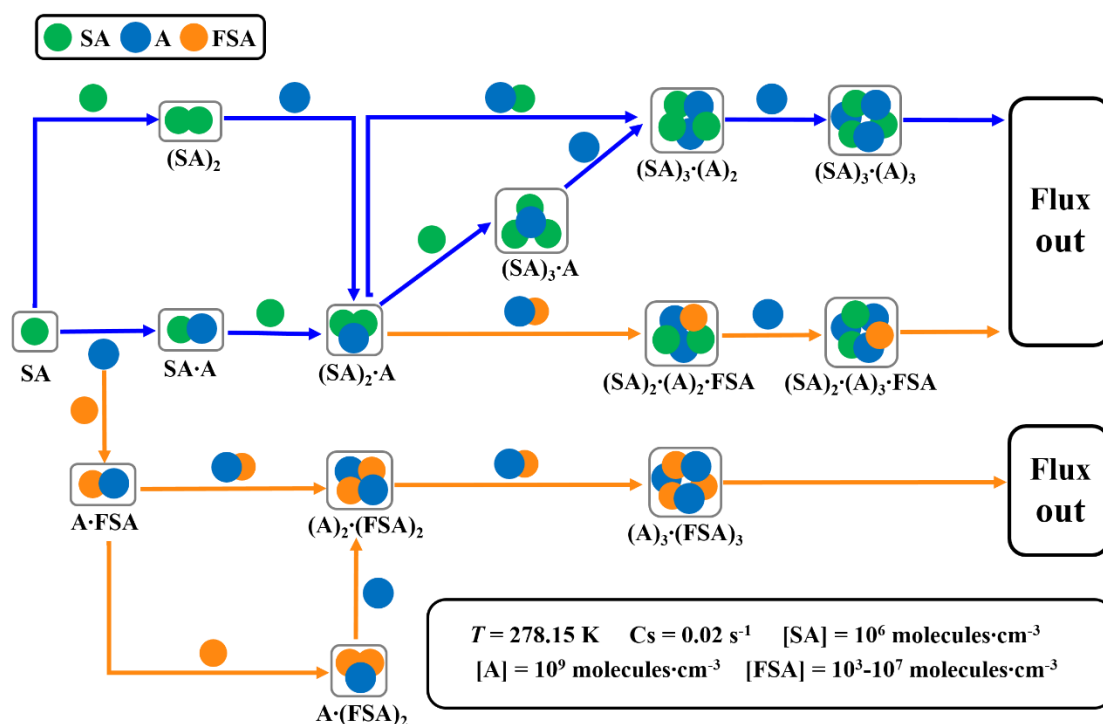
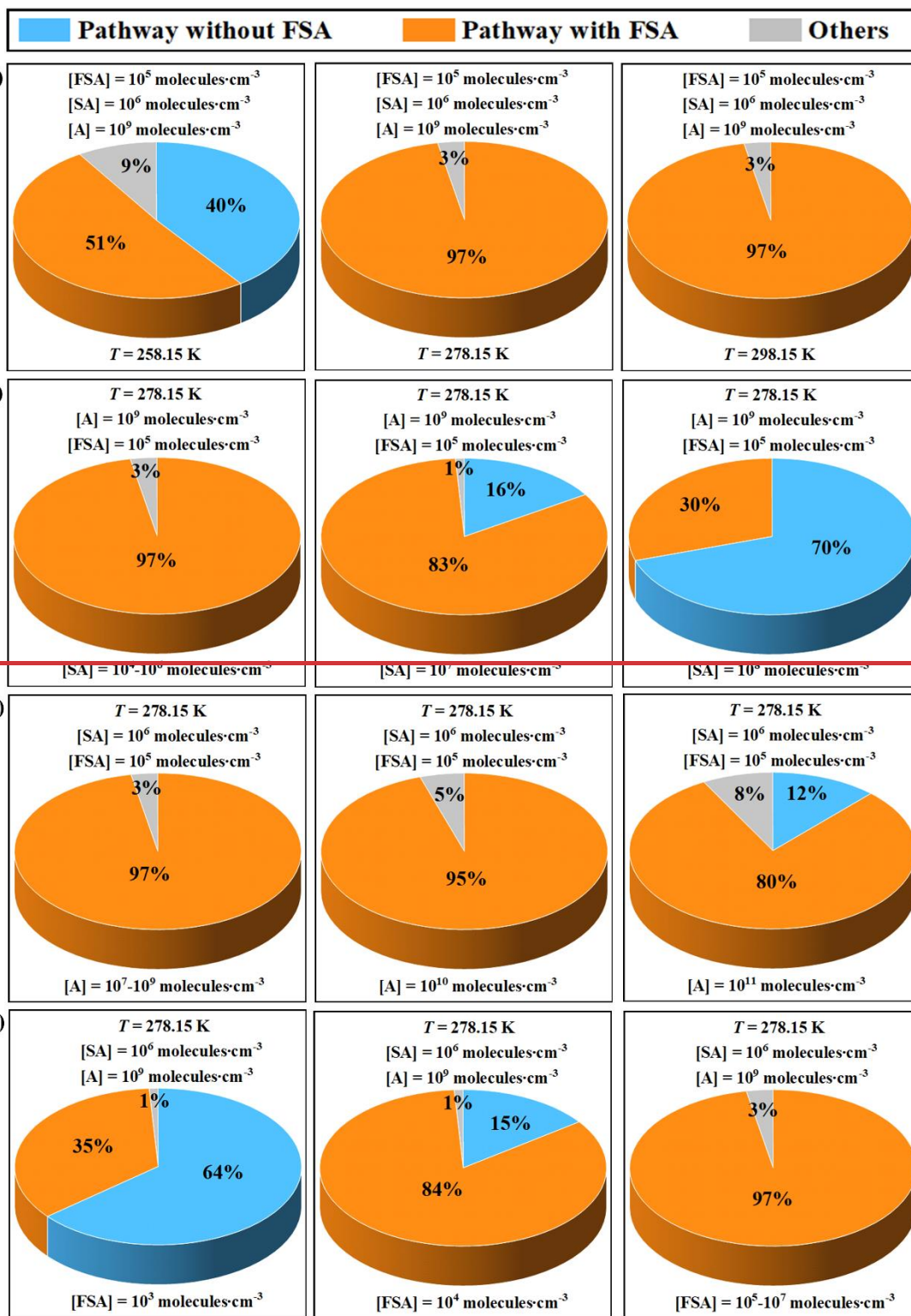


Fig. 8. Primary growth pathways of clusters at $T = 278.15$ K, $[SA] = 10^6$ molecules·cm⁻³, $[A] = 10^9$ molecules·cm⁻³, and $[FSA] = 10^3$ - 10^7 molecules·cm⁻³. Blue and orange arrows represent the SA-A-based and SA-A-FSA-based pathways, respectively.



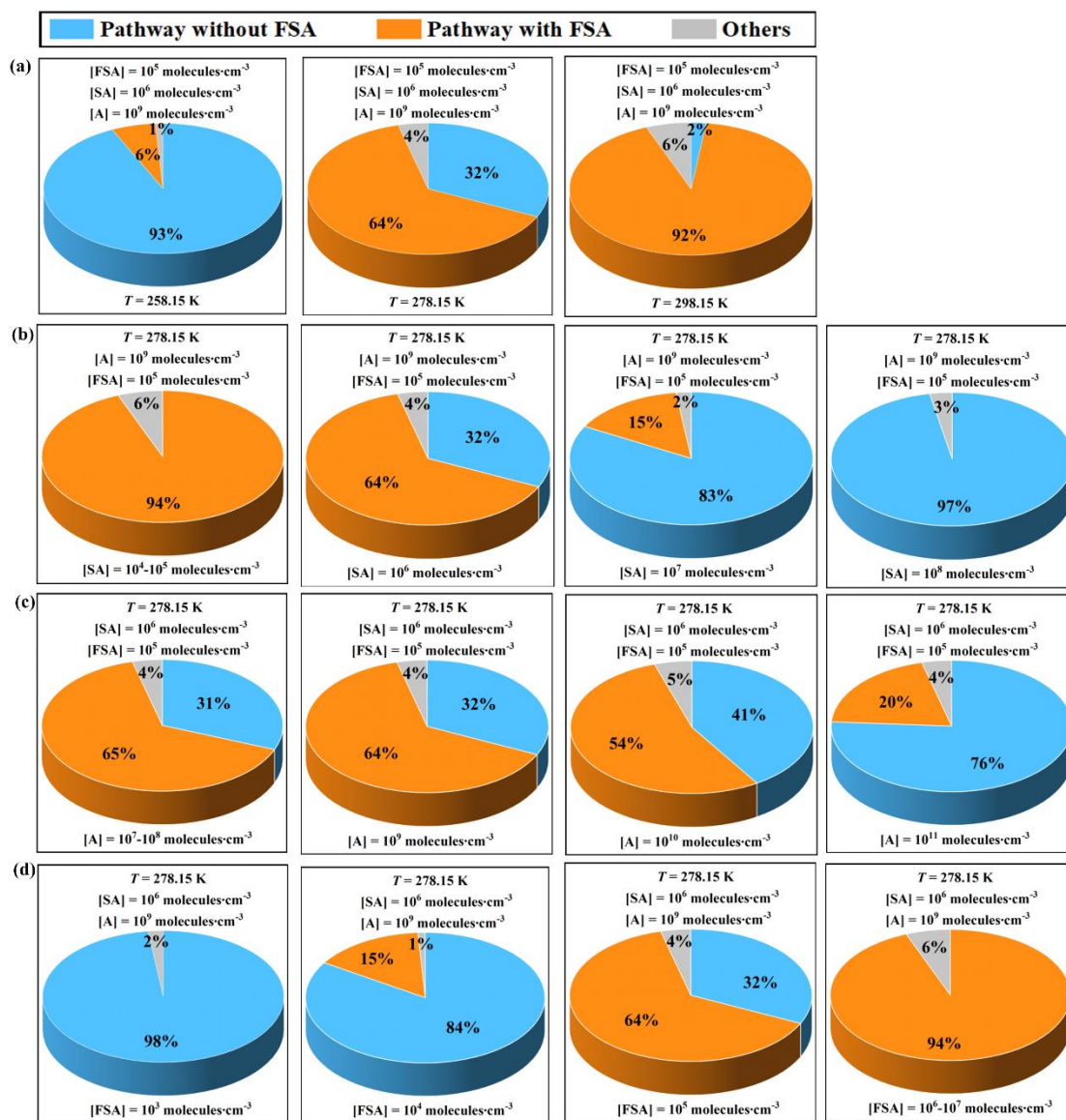


Fig. 9. Influence of (a) temperature, (b) $[SA]$, (c) $[A]$ and (d) $[FSA]$ on the relative contribution of the pure SA-A pathway and the FSA-containing pathway to the flux out of the system.

855 **Table 1.** Rate constants ($\text{cm}^3 \cdot \text{molecule}^{-1} \cdot \text{s}^{-1}$) for SO_3 hydrolysis with and without FSA, H_2O , and X
856 ($X = \text{HNO}_3$, HCOOH , $(\text{COOH})_2$ and H_2SO_4) within the temperature range of 280-320 K

T/K	$k_{\text{SA_FSA}}$	k_{SA}	$k_{\text{SA_WM}}$	$k_{\text{SA_FA}}$	$k_{\text{SA_NA}}$	$k_{\text{SA_OA}}$	$k_{\text{SA_SA}}$
280	7.94×10^{-11}	6.24×10^{-24}	1.68×10^{-12}	8.88×10^{-11}	1.26×10^{-12}	8.02×10^{-11}	5.60×10^{-11}
290	7.84×10^{-11}	8.12×10^{-24}	1.45×10^{-12}	8.17×10^{-11}	1.05×10^{-12}	7.74×10^{-11}	5.08×10^{-11}
298	7.71×10^{-11}	1.02×10^{-23}	1.28×10^{-12}	7.60×10^{-11}	9.11×10^{-13}	7.48×10^{-11}	4.69×10^{-11}
300	7.67×10^{-11}	1.09×10^{-23}	1.24×10^{-12}	7.46×10^{-11}	8.80×10^{-13}	7.42×10^{-11}	4.59×10^{-11}
310	7.46×10^{-11}	1.50×10^{-23}	1.07×10^{-12}	6.78×10^{-11}	7.46×10^{-13}	7.06×10^{-11}	4.13×10^{-11}
320	7.21×10^{-11}	2.12×10^{-23}	9.22×10^{-13}	6.12×10^{-11}	6.46×10^{-13}	6.68×10^{-11}	3.70×10^{-11}

857

Table 2. Binding free energy (kcal·mol⁻¹) for the formation of various clusters at 298 K.

FSA ⁻ -SA	FSA ⁻ -HNO ₃	H ₃ O ⁺ -A	H ₃ O ⁺ -SA	SA-A
-21.2	-12.1	-51.7 (-49.2) ^a	-27.5 (-27.0) ^a	-8.9 (-8.9) ^a
HSO ₄ ⁻ -SA	HSO ₄ ⁻ -(COOH) ₂	HSO ₄ ⁻ -HNO ₃	SA-A-FSA ⁻	SA-A- HOOCCH ₂ COOH
-41.6	-33.6	-27.8	-25.6	-13.1(13.6) ^b
SA-A- HOCCOOSO ₃ H	SA-A- CH ₃ OSO ₃ H	SA-A- HOCH ₂ COOH	SA-A-HOOCCH ₂ CH(NH ₂)COOH	
-20.4 (-22.5) ^c	-18.8 (-20.7) ^d	-13.2 (-14.0) ^e	-12.8 (-13.5) ^f	

Energies are given in kcal·mol⁻¹ and calculated at the M06-2X/6-311++G(2df,2p) level of theory. References are as follows: ^a Zhong et al. (2019), ^b Zhang et al. (2018), ^c Rong et al. (2020), ^d Gao et al. (2023), ^e J. Liu et al. (2021), ^f Zhang et al. (2017).